CrossMark

J. Fluid Mech. (2015), *vol.* 767, *pp.* 735–762. © Cambridge University Press 2015
doi:10.1017/jfm.2015.42

Nonlinear interfacial wave formation in three dimensions

John Grue†

Mechanics Division, Department of Mathematics, University of Oslo, PO Box 1053 Blindern, NO-0316 Oslo, Norway

(Received 26 June 2014; revised 16 January 2015; accepted 19 January 2015; first published online 23 February 2015)

A three-dimensional two-layer, fully dispersive and strongly nonlinear interfacial wave model, including the interaction with a time-varying bottom topography, is developed. The method is based on a set of integral equations. The source and dipole terms are developed in series expansions in the vertical excursions of the interface and bottom topography, obtaining explicit inversion by Fourier transform. Calculations of strongly nonlinear interfacial waves with excursions comparable to the thinner layer depth show that the quadratic approximation of the method contains the essential dynamics, while the additional cubic terms always are small. Computations confirm the onset of wave train formation driven by topography, observed in experiments (Maxworthy, *J. Geophys. Res.*, vol. 84(C1), 1979, pp. 338–346), depending on the Froude number and the topography height. Simulations of tidally driven three-dimensional internal wave formation show the formation of two wave trains per half tidal cycle for strong forcing and one wave train for weak forcing. Waves of both backward and forward curvature are calculated.

Key words: baroclinic flows, geophysical and geological flows, internal waves

1. Introduction

Three-dimensional features of internal gravity waves are observed in field measurements, e.g. Farmer & Armi (1988), Morozov *et al.* (2003), Palmer, Inall & Sharples (2013), remote sensing studies, e.g. Nash & Moum (2005), Jackson *et al.* (2013), Grue (2013*a*), and laboratory experiments, e.g. Maxworthy (1979). Numerical studies using three-dimensional non-hydrostatic ocean models have been employed to calculate the waves, e.g. Fringer, Gerritsen & Street (2006), Berntsen, Xing & Davies (2008), Vlasenko *et al.* (2009), Lai *et al.* (2010), Guo *et al.* (2011) and Zhang, Fringer & Ramp (2011). Use of the rather flexible non-hydrostatic ocean models represents a vital complement to ongoing observational internal wave research in shelf-slope areas, e.g. Vlasenko *et al.* (2013). Field measurements show tidally generated internal wave packets that are highly three-dimensional and of very strong nonlinearity, e.g. Palmer *et al.* (2013). A wave amplitude up to 105 m in shallow parts of the Celtic Sea has been measured (Vlasenko *et al.* 2014).

The ocean models require a discretization of the equations in the three spatial directions. The numerical solution is obtained by solving the pressure Poisson

† Email address for correspondence: johng@math.uio.no

https://doi.org/10.1017/jfm.2015.42 Published online by Cambridge University Press

equation, which is the most expensive part in computational fluid dynamics. Simulations using existing non-hydrostatic ocean models are reported to even take months (Boegman & Dorostkar 2011). Moreover, representation of very short internal waves requires a high resolution in the horizontal plane and may be challenging to fully satisfy (e.g. Vitousek & Fringer 2011).

We here derive a different method for interfacial wave formation in a two-layer fluid. The formulation is based on the boundary integral method (e.g. Mikhlin 1957; Newman 1977, p. 127). The resulting integrals are evaluated by fast Fourier transform in the horizontal plane (Clamond & Grue 2001, § 6). The model is strongly nonlinear and fully dispersive (the whole wavenumber range is accounted for in the continuous model). A formulation with a velocity potential in each layer is adopted. A set of integral equations is derived where the velocity potentials and normal velocities along the lower and upper sides of the interface are connected. Accounting for a bottom variation, an additional integral equation as well as integrals over the bottom variables appear in the formulation. The integral equations are at the onset fully nonlinear in the vertical excursions of the interface and bottom topography. By applying the method of successive approximations, the source and dipole terms of the integral equations are developed in series expansions, containing terms of linear, quadratic, cubic and higher orders. The expansions enable explicit inversion of the integral equations by means of the Fourier transform. The derivations follow previous works for surface wave motion of a one-layer fluid, see Clamond & Grue (2001), Fructus *et al.* (2005*a*), Fructus & Grue (2007). In Grue (2002) the three-dimensional interfacial method was derived mathematically; however, without any bottom variation or complementary numerical implementation and testing of the method.

The successive approximations are here carried out including quadratic and cubic nonlinearity. The quadratic version of the method is very fast and is used for the three-dimensional computations with 0.5×10^6 computational nodes in the horizontal plane. The two-dimensional calculations of the quadratic and cubic versions of the method compare successfully to two-dimensional fully nonlinear reference solutions of solitary waves, for wave amplitudes comparable to and even exceeding the thickness of the thinner layer depth. Transient wave generation calculations using the quadratic and cubic formulations show that the two approximations give the same result for a wave amplitude comparable to the thinner layer depth, thus illustrating the accuracy of the method.

The paper is organized as follows: following the Introduction, § 2 describes the mathematical formulation. By the method of successive approximations, explicit formulae for the normal velocities, sum of the potentials in the two layers along the interface and the potential along the bottom are obtained. Section 3 discusses the time integration of the interfacial elevation and the velocity jump across the interface, taking into account the bottom variation. Numerical tests in two dimensions are given in § 4. Three-dimensional calculations of laboratory experiments carried out by Maxworthy (1979) are obtained in § 5, while wave formation relevant to recent field measurements at Jones Bank (Palmer *et al.* 2013; Vlasenko *et al.* 2013) is calculated in § 6. Rotational effects are not accounted for. Section 7 gives our conclusions.

2. Mathematical formulation

2.1. *Two-fluid model*

The three-dimensional mathematical model, numerical implementation and calculations extend previous works for a single-layer fluid, see Clamond & Grue (2001, § 6),

https://doi.org/10.1017/jfm.2015.42 Published online by Cambridge University Press

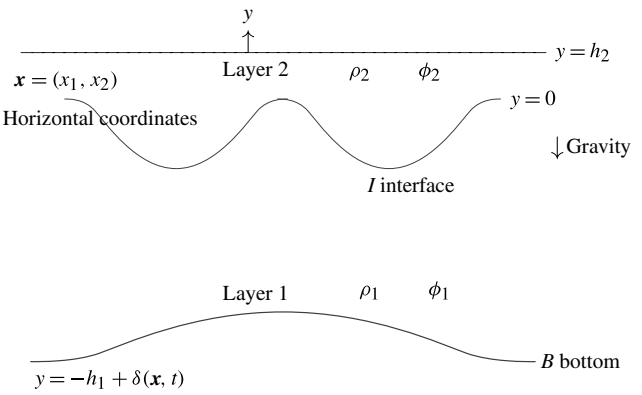


FIGURE 1. Sketch of the two-fluid model.

Grue (2002, § 6), Fructus *et al.* (2005*a*), Fructus & Grue (2007). In Grue (2002) the formulation was developed for the case of a finite depth and extended to a two-layer fluid; however, without a variable bottom and any numerical implementation of the method. This section provides the basis of the mathematical formulation. New extensions of the method are described.

A two-layer model with a different, constant density in each layer is studied (figure 1). The interfacial motion is driven by gravity. Let $\boldsymbol{x} = (x_1, x_2)$ denote horizontal coordinates in the plane that coincides with the interface at rest, y the vertical coordinate and t the time. We denote the densities of the fluids by ρ_1 and ρ_2, where index 1 refers to the lower layer and index 2 to the upper layer. Similarly, the layer depths at rest, far from any variation of the topography, are h_1 and h_2, respectively. Let the position of the interface be determined by $y = \eta(\boldsymbol{x}, t)$. Assuming incompressible and irrotational motion in each of the layers, the fluid motion is governed by the Laplacian potentials ϕ_1 and ϕ_2. The values of the potentials along the interface are introduced as $\phi_{1I}(\boldsymbol{x}, t) = \phi_1(\boldsymbol{x}, y = \eta, t)$ and $\phi_{2I}(\boldsymbol{x}, t) = \phi_2(\boldsymbol{x}, y = \eta, t)$, where indices $1I$ and $2I$ indicate that the potentials are evaluated on the lower and upper side of the interface, respectively, where I denotes the interface. Using a set of differential equations, developed from the kinematic and dynamic boundary conditions at the interface, we integrate forward in time the interfacial elevation and the jump between the potentials at the interface, see § 3 below. Along the interface, the difference and sum of the potentials are introduced as

$$\Psi(\boldsymbol{x}, t) = \phi_{1I}(\boldsymbol{x}, t) - \mu\phi_{2I}(\boldsymbol{x}, t), \quad \Phi(\boldsymbol{x}, t) = \phi_{1I}(\boldsymbol{x}, t) + \phi_{2I}(\boldsymbol{x}, t), \tag{2.1a,b}$$

where $\mu = \rho_2/\rho_1$ denotes the density ratio of the fluids.

The upper boundary of fluid 2 is assumed to be horizontal, in the form of a rigid lid at $y = h_2$. The lower fluid 1 has a bottom variation of $y = -h_1 + \delta(\boldsymbol{x}, t)$. The function δ should be smooth, be of maximum (positive) height smaller than h_1 and decay to zero at infinity.

2.2. *Integral equations*

2.2.1. *The potential in fluid 1*

Solution of the Laplace equation is obtained using Green's theorem. More specifically, for fluid 1, we apply Green's theorem to the velocity potential $\phi_1(\boldsymbol{x}, y)$ and a Green function. This is a three-dimensional source function given by $1/r$, where $r = (R^2 + (y' - y)^2)^{1/2}$ with $R = |(x_1', x_2') - (x_1, x_2)|$ denoting the horizontal distance.

https://doi.org/10.1017/jfm.2015.42 Published online by Cambridge University Press

For convenience we apply $1/r + 1/r_1$ as a Green function, where $1/r_1$ accounts for the image of $1/r$ with respect to $y = -h_1$, i.e. $r_1 = (R^2 + (y' + y + 2h_1)^2)^{1/2}$. Then $(\partial/\partial y)(1/r + 1/r_1) = 0$ on $y = -h_1$. Application of Green's theorem to fluid 1 gives ϕ_1 as

$$\int_S \left[\phi_1' \frac{\partial}{\partial n'}\left(\frac{1}{r} + \frac{1}{r_1}\right) - \frac{\partial \phi_1'}{\partial n'}\left(\frac{1}{r} + \frac{1}{r_1}\right)\right] \mathrm{d}S' = -\alpha \phi_1(\boldsymbol{x}, y), \tag{2.2}$$

where the surface S surrounds fluid 1, and where on the right-hand side $\alpha = 2\pi$ when the evaluation point $(\boldsymbol{x}, y)$ is on the boundary S and $\alpha = 4\pi$ when the evaluation point $(\boldsymbol{x}, y)$ is inside fluid 1, see e.g. Newman (1977, p. 127). In (2.2) n' denotes the unit normal along the integration surface S, pointing out of the fluid, $\mathrm{d}S'$ is a surface element, a prime indicates an integration variable and ϕ_1' means $\phi_1(\boldsymbol{x}', y')$, etc.

The surface S surrounding fluid 1 includes the interface I and bottom boundary B, plus a vertical control surface S_c in the far field. In our applications we assume that there is no motion at infinity, such that there is no contribution over S_c in (2.2). It is possible to account for a constant background horizontal current where the integral over S_c does not contribute. As a consequence, the surface integral in (2.2) is evaluated over the interface I and bottom B. For an evaluation point on the interface I we obtain

$$\int_{I+B}\left(\frac{1}{r} + \frac{1}{r_1}\right)\frac{\partial \phi_1'}{\partial n'}\mathrm{d}S' = 2\pi\phi_1 + \int_{I+B}\phi_1'\frac{\partial}{\partial n'}\left(\frac{1}{r} + \frac{1}{r_1}\right)\mathrm{d}S', \quad (\boldsymbol{x}, y = \eta) \text{ on } I. \tag{2.3}$$

For an evaluation point on the bottom boundary B an equation similar to (2.3) reads:

$$2\pi\phi_1 = \int_{I+B}\left(\frac{1}{r} + \frac{1}{r_{1B}}\right)\frac{\partial \phi_1'}{\partial n'}\mathrm{d}S' - \int_{I+B}\phi_1'\frac{\partial}{\partial n'}\left(\frac{1}{r} + \frac{1}{r_{1B}}\right)\mathrm{d}S', \quad (\boldsymbol{x}, y) \text{ on } B. \tag{2.4}$$

In (2.4) the Green function is chosen as $1/r + 1/r_{1B}$, where $1/r_{1B} = (R^2 + (y' + y)^2)^{-1/2}$ provides the image of $1/r$ with respect to $y = 0$ such that $(\partial/\partial y)(1/r + 1/r_{1B}) = 0$ on $y = 0$.

We employ $\phi_{1I}(\boldsymbol{x}) = \phi_1(\boldsymbol{x}, y = \eta(\boldsymbol{x}))$ along I as introduced in the text above (2.1) and introduce $\phi_{1B}(\boldsymbol{x}) = \phi_1(\boldsymbol{x}, y = -h_1 + \delta(\boldsymbol{x}))$ along B. Scaled normal velocities are introduced as

$$V_I = \frac{\partial \phi_1}{\partial n}\sqrt{1 + |\nabla_H \eta|^2} \quad \text{on } I, \qquad V_B = \frac{\partial \phi_1}{\partial n}\sqrt{1 + |\nabla_H \delta|^2} \quad \text{on } B. \tag{2.5a,b}$$

In (2.5) $\nabla_H = (\partial/\partial x_1, \partial/\partial x_2)$ denotes horizontal gradient; $\mathrm{d}S = \sqrt{1 + |\nabla_H \eta|^2}\mathrm{d}x_1\mathrm{d}x_2$ on I and $\mathrm{d}S = \sqrt{1 + |\nabla_H \delta|^2}\mathrm{d}x_1\mathrm{d}x_2$ on B.

2.2.2. *Leading approximation of the integral equations for fluid 1*

Successive approximations of the integral equations (2.3) and (2.4) are obtained by expanding the Green functions and their derivatives in η and δ. For (2.3), using the expansions obtained in (A 1)–(A 4) in appendix A, the leading approximation of $1/r + 1/r_1$ is given by $1/R + 1/R_1$ in the integration over I, and the leading approximation of $1/r + 1/r_1$ is given by $2/R_0$ in the integration over B. The leading approximation of the normal derivative of the Green function, $(\partial/\partial n')(1/r + 1/r_1)$, is given by $(\partial/\partial(2h_1))(1/R_1)$ in the integration over I, while this term is zero for the integration over B. The leading approximation to (2.3) becomes

$$\int\left(\frac{1}{R} + \frac{1}{R_1}\right)V_I'\mathrm{d}\boldsymbol{x}' + \int\frac{2V_B'}{R_0}\mathrm{d}\boldsymbol{x}' = 2\pi\phi_{1I} + \int\phi_{1I}'\frac{\partial}{\partial(2h_1)}\frac{1}{R_1}\mathrm{d}\boldsymbol{x}', \tag{2.6}$$

https://doi.org/10.1017/jfm.2015.42 Published online by Cambridge University Press

where the integration is over the horizontal plane and $\mathrm{d}\boldsymbol{x}' = \mathrm{d}x_1' dx_2'$. The leading approximation to (2.4) is obtained similarly, using the expansions (A 5)–(A 8) in appendix A, giving

$$2\pi\phi_{1B} = \int \left(\frac{1}{R} + \frac{1}{R_1}\right) V_B' \mathrm{d}\boldsymbol{x}' + \int \frac{2V_I'}{R_0} \mathrm{d}\boldsymbol{x}' - \int \phi_{1B}' \frac{\partial}{\partial(2h_1)} \frac{1}{R_1} \mathrm{d}\boldsymbol{x}', \tag{2.7}$$

where the integration is over the horizontal plane. Equations (2.6) and (2.7) are inverted by means of a Fourier transform. We employ the transform $(R^2 + Y^2)^{-1/2} = \mathscr{F}^{-1}[(2\pi/k)\mathrm{e}^{-\mathrm{i}\boldsymbol{k}\cdot\boldsymbol{x}' - k|Y|}]$, $|Y| \geqslant 0$, where $\mathscr{F}$ denotes Fourier transform, $\mathscr{F}^{-1}$ inverse Fourier transform, $\boldsymbol{k} = (k_1, k_2)$ wavenumber and $k = |\boldsymbol{k}|$. Taking the Fourier transform of (2.6) and (2.7) gives

$$\frac{1 + \mathrm{e}^{-2kh_1}}{k} \mathscr{F}(V_I) + \frac{2\mathrm{e}^{-kh_1}}{k} \mathscr{F}(V_B) = \mathscr{F}(\phi_{1I}) - \mathrm{e}^{-2kh_1} \mathscr{F}(\phi_{1I}), \tag{2.8}$$

$$\mathscr{F}(\phi_{1B}) = \frac{1 + \mathrm{e}^{-2kh_1}}{k} \mathscr{F}(V_B) + \frac{2\mathrm{e}^{-kh_1}}{k} \mathscr{F}(V_I) + \mathrm{e}^{-2kh_1} \mathscr{F}(\phi_{1B}). \tag{2.9}$$

Equations (2.8) and (2.9) express the leading approximation to V_I and ϕ_{1B} in terms of ϕ_{1I} and V_B and are obtained in (2.10) and (2.12) below, respectively.

2.2.3. *Successive approximations of V_I and ϕ_{1B}*

The variable V_I along I and ϕ_{1B} along B are obtained from the full integral equations (2.3) and (2.4) using the method of successive approximations (e.g. Mikhlin 1957). The variables are expanded as $V_I = V_I^{(1)} + V_I^{(2)} + V_I^{(3)} + \cdots$ and $\phi_{1B} = \phi_{1B}^{(1)} + \phi_{1B}^{(2)} + \phi_{1B}^{(3)} + \cdots$. The leading approximations to V_I and ϕ_{1B} are given by $V_I^{(1)}$ and $\phi_{1B}^{(1)}$, respectively, the quadratic approximations by $V_I^{(1)} + V_I^{(2)}$ and $\phi_{1B}^{(1)} + \phi_{1B}^{(2)}$, and the cubic approximations by $V_I^{(1)} + V_I^{(2)} + V_I^{(3)}$ and $\phi_{1B}^{(1)} + \phi_{1B}^{(2)} + \phi_{1B}^{(3)}$, etc. The contributions $V_I^{(1)}, V_I^{(2)}, V_I^{(3)}, \ldots$ and $\phi_{1B}^{(1)}, \phi_{1B}^{(2)}, \ldots$ are obtained, respectively, from (2.3) with the Green function and its derivatives obtained from (A 1)–(A 4) in appendix A, and from (2.4) with the Green function and its derivatives obtained from (A 5)–(A 8), also in appendix A. After some algebra we obtain

$$\mathscr{F}(V_I^{(1)}) = kT_1 \mathscr{F}(\phi_{1I}) - \frac{\mathscr{F}(V_B)}{C_1}, \tag{2.10}$$

$$\mathscr{F}(V_I^{(2)}) = -kT_1 \mathscr{F}(\eta V_I^{(1)}) - \mathrm{i}\boldsymbol{k} \cdot \mathscr{F}(\eta \boldsymbol{\nabla}_H \phi_{1I}) + \frac{\mathrm{i}\boldsymbol{k} \cdot \mathscr{F}(\delta \boldsymbol{\nabla}_H \phi_{1B})}{C_1}, \tag{2.11}$$

where $T_1 = \tanh(kh_1)$ and $C_1 = \cosh(kh_1)$ are introduced. The contribution $V_I^{(3)}$ is obtained in (B 1)–(B 5) in appendix B.

For the potential ϕ_{1B} we obtain

$$\mathscr{F}(\phi_{1B}^{(1)}) = \frac{\mathscr{F}(\phi_{1I})}{C_1} + \frac{T_1 \mathscr{F}(V_B)}{k}, \tag{2.12}$$

$$\mathscr{F}(\phi_{1B}^{(2)}) = -\frac{\mathscr{F}(\eta V_I^{(1)})}{C_1} - \frac{T_1 \mathrm{i}\boldsymbol{k}}{k} \cdot \mathscr{F}(\delta \boldsymbol{\nabla}_H \phi_{1B}) - \mathscr{F}(\delta V_B), \tag{2.13}$$

where in (2.11) and (2.13) $\phi_{1B} = \phi_{1B}^{(1)} + \phi_{1B}^{(2)}$.

https://doi.org/10.1017/jfm.2015.42 Published online by Cambridge University Press

2.2.4. *The potential in fluid 2*

The upper layer is bounded above by a rigid lid at $y=h_2$. The motion in the upper layer is governed by the velocity potential $\phi_2(\boldsymbol{x}, y)$. A scaled normal velocity $W_I = (\partial\phi_2/\partial n)(1+|\boldsymbol{\nabla}_H\eta|^2)^{1/2}$ along I, similar to V_I in (2.5), is introduced, where the normal points into fluid 2. Expanding $W_I = W_I^{(1)} + W_I^{(2)} + W_I^{(3)} + \cdots$ we obtain

$$\mathscr{F}(W_I^{(1)}) = -kT_2\mathscr{F}(\phi_{2I}), \tag{2.14}$$

$$\mathscr{F}(W_I^{(2)}) = kT_2(\eta W_I^{(1)}) - \mathrm{i}\boldsymbol{k}\cdot\mathscr{F}(\eta\boldsymbol{\nabla}_H\phi_{2I}), \tag{2.15}$$

where $T_2=\tanh(kh_2)$ and $\phi_{2I}(\boldsymbol{x})=\phi_2(\boldsymbol{x}, y=\eta)$ along I is used, as introduced in the text above (2.1). The variable $W_I^{(3)}$ is obtained in (B 6)–(B 9) (appendix B).

2.3. *Evaluation of $\Phi=\phi_{1I}+\phi_{2I}$ along the interface*

While the difference potential $\Psi = \phi_{1I} - \mu\phi_{2I}$ is integrated forward in time, see § 3 below, an equation for the sum potential $\Phi = \phi_{1I} + \phi_{2I}$ is required in order to obtain ϕ_{1I} and ϕ_{2I}. Continuity of the normal velocity along the interface gives such an equation, i.e. $V_I = W_I$. Using $V_I = V_I^{(1)} + V_I^{(2)} + V_I^{(3)} + \cdots$ and $W_I = W_I^{(1)} + W_I^{(2)} + W_I^{(3)} + \cdots$ we obtain

$$\begin{aligned} 0 \;=\; & \mathscr{F}(V_I - W_I) = kT_1\mathscr{F}(\phi_{1I}) + kT_2\mathscr{F}(\phi_{2I}) - \frac{\mathscr{F}(V_B)}{C_1} - \mathrm{i}\boldsymbol{k}\cdot\mathscr{F}(\eta\boldsymbol{\nabla}(\phi_{1I}-\phi_{2I})) \\ & - kT_1\mathscr{F}\left[\eta\mathscr{F}^{-1}\left(kT_1\mathscr{F}(\phi_{1I}) - \frac{\mathscr{F}(V_B)}{C_1}\right)\right] + \frac{\mathrm{i}\boldsymbol{k}\cdot\mathscr{F}(\delta\boldsymbol{\nabla}\phi_{1B})}{C_1} \\ & + kT_2\mathscr{F}[\eta\mathscr{F}^{-1}(kT_2\mathscr{F}(\phi_{2I}))] + \mathscr{F}(V_I^{(3)} - W_I^{(3)}) + \cdots . \end{aligned} \tag{2.16}$$

Introducing $\phi_{1I} = (\Psi + \mu\Phi)/(1+\mu)$ and $\phi_{2I} = (\Phi - \Psi)/(1+\mu)$ in (2.16) and multiplying the equation by $(1+\mu)$ we obtain, successively,

$$\Phi = \Phi^{(1)} + \Phi^{(2)} + \Phi^{(3)} + \cdots , \tag{2.17}$$

where the leading contribution is given by

$$\mathscr{F}(\Phi^{(1)}) = \frac{T_2 - T_1}{T_2 + \mu T_1}\mathscr{F}(\Psi) + \frac{(1+\mu)\,\mathscr{F}(V_B)}{k(T_2+\mu T_1)C_1}, \tag{2.18}$$

where V_B is given in (2.5). An improved approximation is given by $\Phi^{(1)}+\Phi^{(2)}$, where $\Phi^{(2)}$ accounts for quadratic coupling and is given by

$$\mathscr{F}(\Phi^{(2)}) = \frac{\mathscr{F}(Q^{(2)})}{k(T_2+\mu T_1)}, \tag{2.19}$$

where

$$\begin{aligned} \mathscr{F}(Q^{(2)}) \;=\; & kT_1\mathscr{F}[\eta\mathscr{F}^{-1}(kT_1\hat{\Psi})] + kT_2\mathscr{F}[\eta\mathscr{F}^{-1}(kT_2\hat{\Psi})] + 2\mu\mathrm{i}\boldsymbol{k}\cdot\mathscr{F}(\eta\boldsymbol{\nabla}\Psi) \\ & - \frac{\mathrm{i}\boldsymbol{k}}{C_1}\cdot\mathscr{F}\left[\delta\mathscr{F}^{-1}\left(\frac{\mathrm{i}\boldsymbol{k}\hat{\Psi}}{C_1}\right)\right] - (1+\mu)\left[kT_1\mathscr{F}\left[\eta\mathscr{F}^{-1}\left(\frac{\mathscr{F}(V_B)}{C_1}\right)\right]\right. \\ & \left. + \frac{\mathrm{i}\boldsymbol{k}}{C_1}\cdot\mathscr{F}\left[\delta\mathscr{F}^{-1}\left(\frac{\mathrm{i}\boldsymbol{k}}{k}T_1\mathscr{F}(V_B)\right)\right]\right] \end{aligned}$$

https://doi.org/10.1017/jfm.2015.42 Published online by Cambridge University Press

$$+\mu kT_1\mathscr{F}[\eta\mathscr{F}^{-1}(kT_1\hat{\Phi})]-kT_2\mathscr{F}[\eta\mathscr{F}^{-1}(kT_2\hat{\Phi})]+(\mu-1)\mathrm{i}\boldsymbol{k}\cdot\mathscr{F}(\eta\nabla\Phi)$$
$$-\frac{\mu\mathrm{i}\boldsymbol{k}}{C_1}\cdot\mathscr{F}\left[\delta\mathscr{F}^{-1}\left(\frac{\mathrm{i}\boldsymbol{k}\hat{\Phi}}{C_1}\right)\right], \tag{2.20}$$

where on the right-hand side of (2.20) $\Phi=\Phi^{(1)}+\Phi^{(2)}$ and the value of $\Phi^{(2)}$ is obtained iteratively. In (2.20) we have for simplicity set $\hat{\Psi}=\mathscr{F}(\Psi)$ and $\hat{\Phi}=\mathscr{F}(\Phi)$. Terms including cubic couplings are obtained as

$$\mathscr{F}(\Phi^{(3)})=\frac{\mathscr{F}(Q^{(3)})}{k(T_2+\mu T_1)}, \tag{2.21}$$

where

$$\mathscr{F}(Q^{(3)})=-(1+\mu)\left(\frac{\mathrm{i}\boldsymbol{k}\cdot\mathscr{F}(\delta\nabla\phi_{1B}^{(2)})}{C_1}+\mathscr{F}(V_I^{(3)}-W_I^{(3)})\right). \tag{2.22}$$

The velocities $V_I^{(3)}$ and $W_I^{(3)}$ are given in (B 1) and (B 6) in appendix B, respectively, while $\phi_{1B}^{(2)}$ is given in (2.13).

3. Interfacial motion

3.1. *Time integration*

The kinematic boundary condition at the interface gives

$$\eta_t-V_I=0\quad\text{at } I, \tag{3.1}$$

where V_I is given in (2.5). Alternatively, W_I given in the text above (2.14) and (2.15) may be used. In the numerical implementation we use $(V_I+W_I)/2$ in (3.1).

The pressure in each of the fluids is obtained from the Bernoulli equation, giving $p_j=-\rho_j[\partial\phi_j/\partial t+|\boldsymbol{v}_j|^2/2+gy]+\text{const.}$, where $\boldsymbol{v}_j=\nabla\phi_j$ $(j=1,2)$ (note that we use ∇_H for the horizontal gradient). At the interface, the pressure is expressed in terms of ϕ_{jI}, V_I and η by (see Grue 2002)

$$p_j=-\rho_j\left[\phi_{jI,t}+g\eta+\frac{1}{2}\frac{|\nabla_H\phi_{jI}|^2-V_I^2-2V_I\nabla_H\eta\cdot\nabla_H\phi_{jI}+|\nabla_H\eta\times\nabla_H\phi_{jI}|^2}{1+|\nabla_H\eta|^2}\right]+\text{const.}, \tag{3.2}$$

$(j=1,2)$. Continuity of the pressure at the interface gives, disregarding the effect of interface tension,

$$(\phi_{1I}-\mu\phi_{2I})_t+g'\eta=\mathscr{NL}_2,\quad\text{at } I, \tag{3.3}$$

$$\mathscr{NL}_2=-\frac{|\nabla_H\phi_{1I}|^2-\mu|\nabla_H\phi_{2I}|^2-(1-\mu)V_I^2}{2+2|\nabla_H\eta|^2}$$
$$-\frac{-2V_I\nabla_H\eta\cdot\nabla_H(\phi_{1I}-\mu\phi_{2I})+|\nabla_H\eta\times\nabla_H\phi_{1I}|^2-\mu|\nabla_H\eta\times\nabla_H\phi_{2I}|^2}{2+2|\nabla_H\eta|^2}, \tag{3.4}$$

where in (3.3) $g'=(1-\mu)g$ denotes reduced gravity.

In the case of linear waves moving along a fluid of constant depth, i.e. the bottom of fluid 1 is located at $y=-h_1$, the vertical velocities of the lower and upper fluid

https://doi.org/10.1017/jfm.2015.42 Published online by Cambridge University Press

along the interface are given by $\mathscr{F}(V_I^{(1)}) = kT_1\mathscr{F}(\phi_{1I})$ and $\mathscr{F}(W_I^{(1)}) = -kT_2\mathscr{F}(\phi_{2I})$, respectively, see the derivations in §§ 2.2.2–2.2.4; in particular (2.10) and (2.14), where in the former $V_B = 0$ for a flat bottom. The sum gives

$$\frac{\mathscr{F}(V_I^{(1)})}{kT_1} + \frac{\mu\mathscr{F}(W_I^{(1)})}{kT_2} = \mathscr{F}(\Psi) = \mathscr{F}(\phi_{1I} - \mu\phi_{2I}), \tag{3.5}$$

where the difference potential Ψ is given in (2.1). A pseudo-vertical velocity $V_I^{(lin)}$ is defined, satisfying

$$\left(\frac{1}{kT_1} + \frac{\mu}{kT_2}\right)\mathscr{F}(V_I^{(lin)}) = \mathscr{F}(\Psi), \tag{3.6}$$

giving $\mathscr{F}(V_I^{(lin)}) = \omega^2\mathscr{F}(\Psi)/g'$, where ω^2 is defined as

$$\omega^2 = \frac{g'kT_1T_2}{T_2 + \mu T_1}. \tag{3.7}$$

Note that V_I^{lin} differs from $V_I^{(1)}$ and $W_I^{(1)}$, and further that ω^2 appears through a definition from the analysis leading to (3.6). Equation (3.7) corresponds to the usual dispersion relation for linear interfacial waves in a two-layer fluid; this dispersion relation is real (no imaginary part). In the limit $kh_1, kh_2 \to 0$ we obtain

$$c_0^2 = \frac{\omega^2}{k^2} = \frac{g'h_1h_2}{h_2 + \mu h_1}. \tag{3.8}$$

This defines the linear long-wave speed of the two-layer fluid.

The linear part of the prognostic equations is integrated analytically. This enhances the accuracy of the time integration such that a moderate time step can be used. Introducing dimensionless variables $\mathscr{F}(\Psi^*) = (\omega/g'h_2)\mathscr{F}(\Psi)$, $\eta^* = \eta/h_2$ and $t^* = tc_0/h_2$, the Fourier transforms of (3.1) and (3.3) become

$$\mathscr{F}(\eta^*)_{t^*} - \omega^*\mathscr{F}(\Psi^*) = \mathscr{F}(\mathscr{R}_1), \tag{3.9}$$

$$\mathscr{F}(\Psi^*)_{t^*} + \omega^*\mathscr{F}(\eta^*) = \mathscr{F}(\mathscr{R}_2), \tag{3.10}$$

where $\mathscr{F}(\mathscr{R}_1) = \mathscr{F}(V_I - V_I^{(lin)})/c_0$, $\mathscr{F}(\mathscr{R}_2) = (\omega c_0/g')\mathscr{F}(\mathscr{N}\mathscr{L}_2/c_0^2)$ and $(\,)_{t^*}$ denotes time derivative. V_I, W_I are obtained successively from (2.10)–(2.11), (2.14)–(2.15) and (B 1), (B 6) in appendix B. The right-hand side $\mathscr{N}\mathscr{L}_2$ is obtained from (3.4).

In $V_I^{(1)}$, the contribution from V_B, see (2.10), is obtained from the bottom boundary condition. In the case of a moving bottom we obtain

$$\delta_t + V_B = 0 \quad \text{at } y = -h_1 + \delta. \tag{3.11}$$

In the special case when the bottom topography is moving with a horizontal velocity $\boldsymbol{U}(t)$ we obtain $\delta_t = -\boldsymbol{U}(t)\cdot\boldsymbol{\nabla}_H\delta$, giving $V_B = \boldsymbol{U}(t)\cdot\boldsymbol{\nabla}_H\delta$. For a rigid, non-moving bottom, $V_B = 0$.

Regarding initial conditions, the fluid and bottom velocities are zero at $t = 0$ in the present applications, except for the time stepping of the solitary waves in § 4.2 below, where the wave motion and potentials in the constant depth case are specified at $t = 0$.

https://doi.org/10.1017/jfm.2015.42 Published online by Cambridge University Press

3.1.1. *Other forcing mechanisms. Coriolis force*

Forcing mechanisms other than moving the bottom geometry are possible, e.g. prescribing a pressure at the upper boundary. However, that would imply a reformulation of the kinematic (and dynamic) boundary conditions at the upper boundary.

Wave diffraction of a slowly rotating geometry, accounting for the effect of the non-Newtonian Coriolis force, has been formulated via potential theory by Grue & Palm (1996). The perturbation analysis developed in the frequency domain was performed for a single-layer fluid and may be extended to the two-layer case. The present time integration formulation may not be directly suitable for including the effect of the Coriolis force. A problem is connected to the periodic extensions at the boundaries of the horizontal computational domain.

Thus, the present model and simulations of a field experiment, see § 6, do not take into account rotational effects, which are present in any realistic oceanic setting, particularly at high latitudes. While the wave generation during a short time frame, using the present method, may be realistic, the subsequent wave evolution is modified by rotational effects, where an additional term appears in the dispersion relation (e.g. Grimshaw & Helfrich 2012, their equation (6)). See also Ostrovsky (1978). Such an additional rotational correction is not accounted for in the dispersion relation in the present model, see (3.7).

3.2. *Numerical implementation*

Equations (3.9)–(3.10) in matrix form read $\mathscr{F}(Y)_t + \boldsymbol{A}\mathscr{F}(Y) = \mathscr{F}(\mathscr{R})$, where $Y = [\eta, \Psi]^{\mathrm{T}}$, $\mathscr{R} = [\mathscr{R}_1, \mathscr{R}_2]^{\mathrm{T}}$, with $[\,]^{\mathrm{T}}$ denoting transpose. The symbols with stars are omitted in what follows. The matrix $\boldsymbol{A}$ and its variant $\mathrm{e}^{\boldsymbol{A}(t-t_0)}$ are given by

$$\boldsymbol{A} = \begin{bmatrix} 0 & -\omega \\ \omega & 0 \end{bmatrix}, \quad \mathrm{e}^{\boldsymbol{A}(t-t_0)} = \begin{bmatrix} \cos\omega(t-t_0) & -\sin\omega(t-t_0) \\ \sin\omega(t-t_0) & \cos\omega(t-t_0) \end{bmatrix}. \tag{3.12a,b}$$

The equation

$$\mathscr{F}(Z)_t = \mathrm{e}^{\boldsymbol{A}(t-t_0)}\mathscr{F}(\mathscr{R}) \tag{3.13}$$

is integrated forward in time using a fourth-order Runge–Kutta scheme with a constant time step, where

$$\mathscr{F}(Y) = \mathrm{e}^{-\boldsymbol{A}(t-t_0)}\mathscr{F}(Z) \tag{3.14}$$

provides the relation between the Y-variable and the auxiliary Z-variable, obtained by integrating (3.13). In (3.13) and (3.14) t_0 means the time of the previous time step, or the starting time of the time integration. At each time step the variables η and Ψ are used as input to obtain Φ, whereby the potentials ϕ_{1I} and ϕ_{2I} are evaluated. The velocities V_I, W_I and the right-hand side $\mathscr{R} = [\mathscr{R}_1, \mathscr{R}_2]^{\mathrm{T}}$ are then obtained. The time integration using (3.13) yields the linear part analytically, implying that the relatively small nonlinear terms on the right-hand side can be dealt with using a relatively moderate time step.

The method is used for two- and three-dimensional calculations. In the two-dimensional implementation, a wave tank of length L_1 has N_1 nodes, giving $\Delta x_1 = L_1/N_1$. The wavenumber vector in spectral space reads $(0, \Delta k_1, 2\Delta k_1, \ldots, (N_1/2-1)\Delta k_1, -(N_1/2)\Delta k_1, \ldots, -\Delta k_1)$, where $\Delta k_1 = 2\pi/L_1$. A MATLAB script with MATLAB FFT routines is used in the two-dimensional calculations. The three-dimensional calculations, using a Fortran code (§§ 5 and 6 below), employ

https://doi.org/10.1017/jfm.2015.42 Published online by Cambridge University Press

a rectangular wave tank of length L_1 and width L_2, discretized with $N_1 \times N_2$ nodes, with $(\Delta x_1,\ \Delta x_2) = (L_1/N_1,\ L_2/N_2)$ and $(\Delta k_1,\ \Delta k_2) = (2\pi/L_1,\ 2\pi/L_2)$. Each product between two physical variables is transformed to Fourier space, where the upper half of the spectrum is set to zero (zero-padding). The result is then transformed back into the physical space. No smoothing is applied. The number of operations in the method is governed by the number of FFT operations, which is $O(N_0 \log N_0)$, where $N_0 = N_1 \times N_2$ is the number of nodes in the calculations. Further comments on the calculation procedures and efficiency are given in § 4.3 below.

4. Numerical experiments in two dimensions

4.1. *Numerical calculations of* Φ

The accuracy and convergence of the successive approximations of the potential Φ obtained in (2.17) (see § 2.3) are investigated through numerical examples. First we perform a set of computations of interfacial solitary waves of finite, moderate and large amplitude. Available reference solutions using the fully nonlinear and dispersive method documented in Grue *et al.* (1999) give $\Psi = \phi_{1I} - \mu\phi_{2I}$ and the elevation η. These are used as input to the calculations of the various approximations of Φ. The bottom of fluid 1 is at $y_1 = -h_1$.

Solitary depression waves of amplitude up to twice the upper layer depth for $h_1/h_2 = 6$ and $1 - \rho_2/\rho_1 \ll 1$ are obtained ($|x_1| < 100h_2, N_1 = 400$). Calculations using the quadratic approximation $\Phi \simeq \Phi^{(1)} + \Phi^{(2)}$, with $\Phi^{(1)}$ obtained from (2.18) and $\Phi^{(2)}$ from (2.19) and (2.20), fit to the fully nonlinear reference solution, within graphical accuracy, for the solitary wave amplitudes a_0/h_2 of 0.5, 1, 1.6 and 2. This illustrates the rapid convergence of the successive approximations employed in the calculations. The results in figure 2 are shown for x_1-values between 0 and $40h_2$, where $x_1 = 0$ refers to the point of maximum amplitude of the solitary waves. Interfacial profiles are visualized in figure 4 for $a_0/h_2 = 0.5$ and 1. Calculations using only $\Phi^{(1)}$, obtained from (2.18), give results quite far from the exact solution, even for the moderately small amplitude of $a_0/h_2 = 0.5$. The difference between $\Phi^{(1)}$ and the numerically exact Φ increases with increasing amplitude, becoming very large when $a_0/h_2 = 2$ (figure 2*d*).

The convergence of the successive approximations is further explored by comparing numerical values of $\Phi^{(1)} + \Phi^{(2)}$ and $\Phi^{(1)} + \Phi^{(2)} + \Phi^{(3)}$. In figure 3(*a*) the two approximations are compared for $a_0/h_2 = 0.8$, which is a typical amplitude of the time simulations performed below. Both $\Phi^{(1)} + \Phi^{(2)}$ and $\Phi^{(1)} + \Phi^{(2)} + \Phi^{(3)}$ are very close to the reference solution, which means that $\Phi^{(3)}$ is very small. Only a small part of the computational domain, from the point of maximal depression at $x_1 = 0$ to $x_1/h_2 = 20$, is visualized.

We also calculate the solitary waves with another reference depth of the layers, with a modified upper layer depth of $\tilde{h}_2 = h_2 + h_0$, lower layer depth of $\tilde{h}_1 = h_1 - h_0$ and elevation of $\tilde{\eta} = \eta + h_0$. The calculations further illustrate the contributions from the quadratic and cubic approximations. The results for the same solitary wave amplitude of $a_0/h_2 = 0.8$, with $h_0/h_2 = 1$, show that $\Phi^{(1)} + \Phi^{(2)} + \Phi^{(3)}$ now compares somewhat better than $\Phi^{(1)} + \Phi^{(2)}$ to the reference at the peak value of $\mathscr{F}^{-1}(k\mathscr{F}(\Phi))/c_0$ at $x_1/h_2 \sim 7$–8 (figure 3*b*) (where c_0 is defined in (3.8)). The difference between the approximations is extremely small for the other x_1-values. The same convergence and small difference between the approximations and the reference solution are obtained also for the amplitudes of $a_0/h_2 = 1.6$ and 2, see figure 3(*c*,*d*). Calculations of solitary waves of very large amplitude, for a layer depth of $h_1/h_2 = 20.4$, show that

https://doi.org/10.1017/jfm.2015.42 Published online by Cambridge University Press

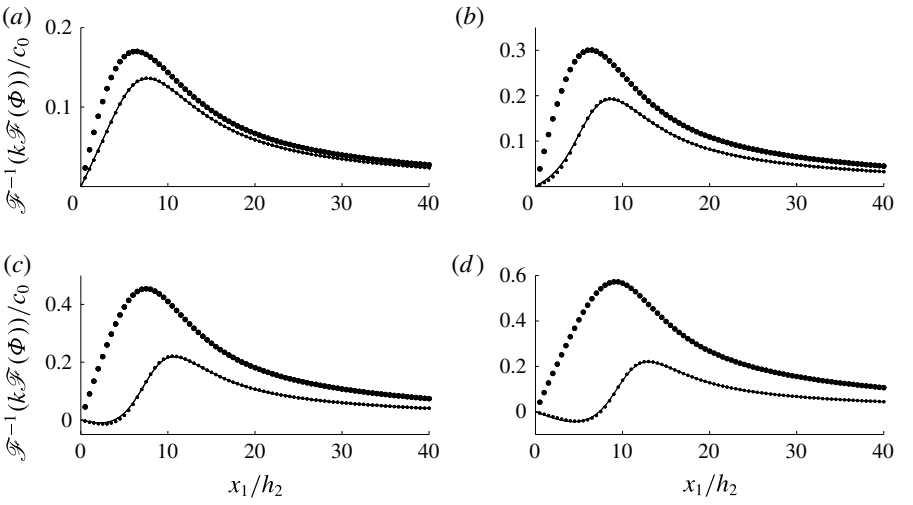


FIGURE 2. Calculation of the potential $\mathscr{F}^{-1}(k\mathscr{F}(\Phi))/c_0 = \mathscr{F}^{-1}(k\mathscr{F}(\phi_{1I} + \phi_{2I}))/c_0$ for solitary depression waves of amplitude a_0. Elevation η and $\phi_1 - \mu\phi_2$ given as input. $\Phi^{(1)}$ obtained from (2.18) (●), $\Phi^{(1)} + \Phi^{(2)}$ with $\Phi^{(2)}$ obtained from (2.19) to (2.20) (●), fully nonlinear (exact) reference computation (——). (*a*) $a_0/h_2 = 0.5$; (*b*) $a_0/h_2 = 1$; (*c*) $a_0/h_2 = 1.6$; (*d*) $a_0/h_2 = 2$. $h_1/h_2 = 6$, $\mu = 1$. $\Delta x_1/h_2 = 0.5$.

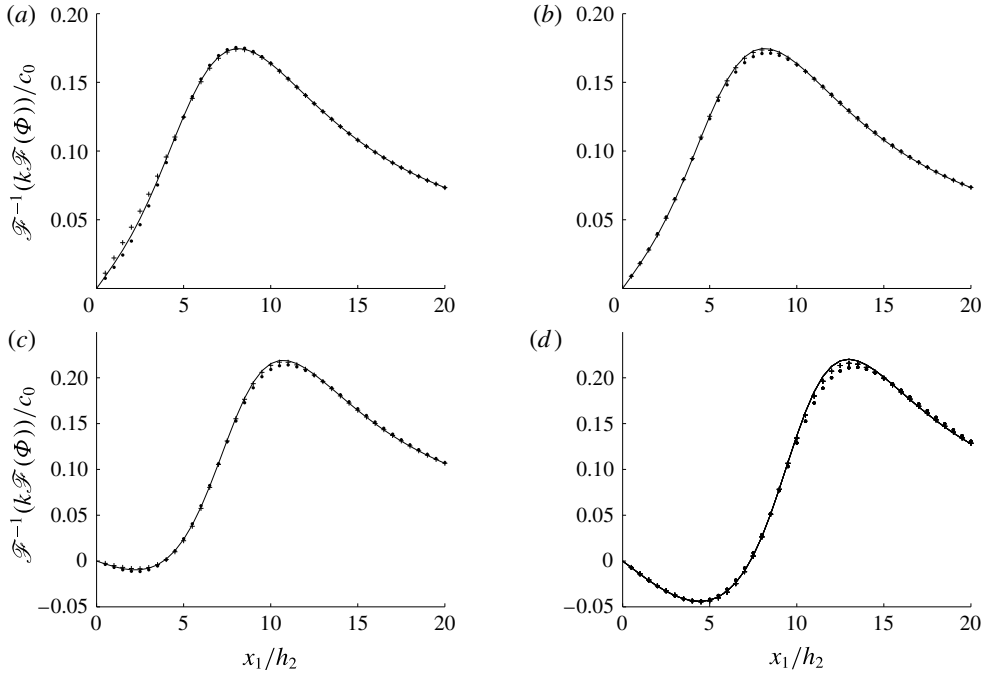


FIGURE 3. Same as figure 2. Quadratic (●), cubic (+), fully nonlinear (exact) (——). (*a*) $a_0/h_2 = 0.8$, $h_0 = 0$; (*b*) $a_0/h_2 = 0.8$, $h_0/h_2 = 1$; (*c*) $a_0/h_2 = 1.6$, $h_0/h_2 = 1$; (*d*) $a_0/h_2 = 2$, $h_0/h_2 = 1.5$. $h_1/h_2 = 6$, $\mu = 1$, $\Delta x_1/h_2 = 0.5$.

https://doi.org/10.1017/jfm.2015.42 Published online by Cambridge University Press

	Propagation distance $117h_2$			Propagation distance $129h_2$		
	a/h_2	c/c_0	Number of time steps	a/h_2	c/c_0	Number of time steps
FNL	0.5000	1.1680	—	1	1.2858	—
Quadratic	0.5063	1.1682	20 030	1.0175	1.2865	20 054
Cubic	0.4992	1.1679	20 036	0.9969	1.2859	20 065

TABLE 1. Time stepping of solitary waves of amplitude $a_0/h_2 = 0.5$ and 1, using fully nonlinear (FNL) (Grue *et al.* 1999), quadratic and cubic calculations with time step $\Delta tc_0/h_2 = 0.005$.

the quadratic approximation $V_I^{(1)} + V_I^{(2)}$ is excellent for amplitudes even as large as $a_0/h_2 = 5$. Similar calculations of $W_I^{(1)} + W_I^{(2)}$ are also excellent (Grue 2013*b*).

Two important conclusions can be drawn from the calculations in this subsection:

(i) Φ obtained from the quadratic approximation $\Phi^{(1)} + \Phi^{(2)}$ provides a very accurate evaluation of the sum potential for solitary waves of amplitude $a_0/h_2 = O(1)$, when compared to the fully nonlinear reference solution. This is the relevant range of amplitudes for the time simulations of waves generated at a three-dimensional topography. (For comparison to approximations using the KdV equation, see § 4.4.)

(ii) Calculations including the cubic approximation show that $\Phi^{(3)}$ is much smaller than $\Phi^{(1)} + \Phi^{(2)}$ and illustrate the rapid convergence and usefulness of the successive approximations in the interfacial wave calculations.

4.2. *Time simulations in two dimensions*

Time integration of solitary wave propagation during 2×10^4 time steps of $\Delta tc_0/h_2 = 0.005$ shows that the quadratic and cubic approximations compare excellently to the fully nonlinear solution (Grue *et al.* 1999), for amplitudes of $a_0/h_2 = 0.5$ and 1, depth ratio $h_1/h_2 = 6$ and density ratio $1 - \rho_2/\rho_1 \ll 1$ (table 1, figure 4).

The interfacial motion driven by an oscillating two-dimensional bump on the bottom is shown in figure 5. The bottom topography has shape $\delta(\boldsymbol{x}, t) = d_m(1 + \tanh((x_1 - x_1^a)/3.5h_2))(1 + \tanh((x_1^b - x_1)/3.5h_2))/4$, where d_m denotes the maximum height and $x_1^b - x_1^a = 34h_2$. The bottom topography is moved in a sinusoidal manner with a horizontal velocity of $U(t) = U_m \sin \Omega t$, starting from rest. The figure shows the formation of interfacial waves after time $\Omega t = 3\pi/2$, corresponding to three-quarters of a total period of oscillation. The value of $\Omega h_2/c_0$ is 1/70, relevant to the three-dimensional calculations in §§ 5 and 6 below. Two different topography heights d_m, two different layer depths and two different Froude numbers (0.5 and 0.7) are tested. The interfacial wave trains attain a local wave height comparable to the upper layer depth h_2. The results in figure 5 show that both the quadratic and cubic approximations give an excellent representation of the wave generation due to oscillatory motion of the topography. The rapid convergence and usefulness of the successive approximations are illustrated. In figure 5 we have also included calculations using the linear approximation, where no nonlinear coupling terms are included, giving numerical solutions with no wave formation.

4.3. *Comments on the calculation procedures and efficiency*

The results illustrate the accuracy of the quadratic and cubic approximations in obtaining interfacial waves with amplitudes up to unity. Moreover, the differences

https://doi.org/10.1017/jfm.2015.42 Published online by Cambridge University Press

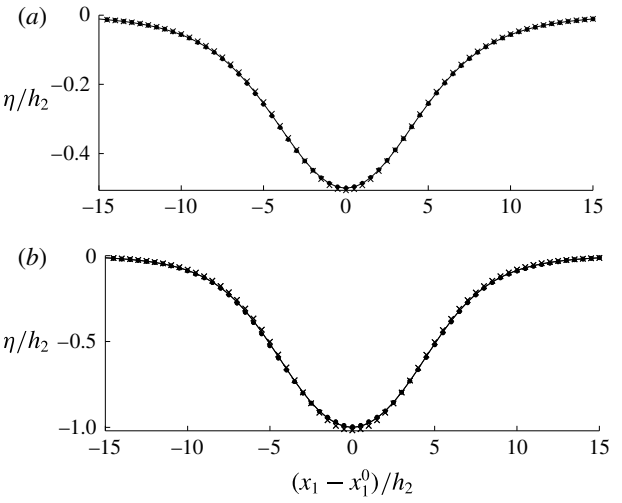


FIGURE 4. Solitary waves of depression integrated forward a distance x_0. Quadratic approximation ($\times$), cubic approximation (●), reference (——). (*a*) Amplitude $a_0/h_2 = 0.5$, $x_1^0/h_2 = 117$, number of time steps: 20 030 (quadratic); 20 036 (cubic). (*b*) Amplitude $a_0/h_2 = 1$, $x_1^0/h_2 = 129$, number of time steps: 20 054 (quadratic); 20 065 (cubic). $\Delta x_1/h_2 = 0.5$, $\Delta t c_0/h_2 = 0.005$, $h_1/h_2 = 6$, $\rho_2/\rho_1 = 1$.

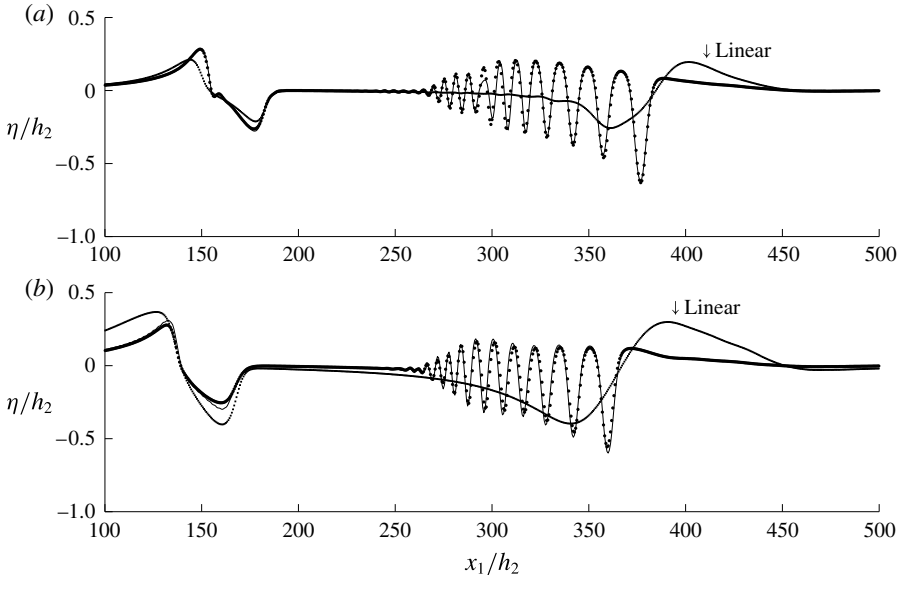


FIGURE 5. Elevation η at $t = (3\pi/2)/\Omega$ with cubic (——), quadratic (●) and linear approximation (■) driven by a moving bottom topography for (*a*) $U_0/c_0 = 0.7$, $h_1 = 4h_2$, $d_m/h_2 = 1$; (*b*) $U_0/c_0 = 0.5$, $h_1 = 6h_2$, $d_m/h_2 = 2.5$. Motion of bottom topography: $U(t) = U_0 \sin \Omega t$, $\Omega h_2/c_0 = 1/70$, $\rho_2/\rho_1 = 1$. RK4 with $\Delta t c_0/h_2 = 0.0825$, 4000 time steps, $L = 600$, $N = 1000$. Bottom shape: $\delta(x_1, t) = d_m((1/2) + (\tanh((x_1 - x_1^a)/3.5h_2))/2)((1/2) + (\tanh((x_1^b - x_1)/3.5h_2))/2)$. Initially, $x_1^a = 100h_2$, $x_1^b = 134h_2$.

https://doi.org/10.1017/jfm.2015.42 Published online by Cambridge University Press

between the quadratic and cubic calculations are very small. Use of the quadratic approximation requires fewer products and temporal variables than the cubic approximation. This is beneficial in the three-dimensional calculations, where the available RAM represents a practical limitation on the maximum number of variables. In the three-dimensional version of the method implemented in Fortran we employ the quadratic approximation using $\Phi \simeq \Phi^{(1)} + \Phi^{(2)}$, $V_I \simeq V_I^{(1)} + V_I^{(2)}$ and $W_I \simeq W_I^{(1)} + W_I^{(2)}$. With the streamlined Fortran code we employ $N_0 = 720 \times 720 \simeq 0.5 \times 10^6$ calculation nodes in the horizontal plane on a Lenovo T430 Thinkpad. Calculations using 720×720 and 500×500 nodes take 6 and 2.2 s per time step, respectively, confirming the computational demands are $O(N_0 \log N_0)$, as mentioned at the end of § 3.2.

We note that, for surface waves, Fructus *et al.* (2005*a*) have fully tested the numerical implementation of the cubic version, including the full representation of the remaining integrals appearing in the exact integral equation formulation, where the remaining integrals decay rapidly in space, implying only local integration of these integrals is required rather than evaluation over the entire horizontal plane. Moreover, Clamond, Fructus & Grue (2007) tested time integrators, varying the time step – with the accuracy depending on the local nonlinearity – also for surface waves. Three-dimensional surface wave patterns were obtained by Fructus *et al.* (2005*b*) using up to $N_0 = 10^4$ nodes, much smaller than the present three-dimensional interfacial calculations using $N_0 = 0.5 \times 10^6$ nodes.

4.4. *Comparison to the KdV equation*

The present method is fully dispersive, as it resolves the entire wavenumber spectrum up to the truncation. While the variables are represented along the exact position of the interface and bottom variation, accounting thus for an important part of the nonlinearity, the integral equations giving V_I and W_I along I and ϕ_{1B} along B are approximated, here retaining the quadratic and cubic approximations. The method differs fundamentally from the KdV equation or its extensions, where the KdV equation is valid in the long-wave range. Specifically, interfacial KdV solitons (sech^2-profiles) differ fundamentally from the fully nonlinear interfacial waves when the amplitude exceeds 0.4 times the thinner layer depth, as visualized by Grue *et al.* (1999). For surface waves, the present method and the KdV equation have been used to calculate fission of the 2004 Indian Ocean tsunami in the shallow Strait of Malacca, finding that the KdV equation has limited capacity in resolving dispersion in comparison with the fully dispersive method (Grue *et al.* 2008). For interfacial solitary waves, the KdV equation is found to be valid up to a wave amplitude of $a/h_2 = 0.4$ (Grue *et al.* 1999). The two-dimensional, fully nonlinear interfacial calculations of Grue *et al.* (1997) obtained very good agreement with laboratory experiments on unsteady transcritical two-layer flow over a bottom topography, where bad agreement with weakly nonlinear interfacial KdV theories was reported (Melville & Helfrich 1987).

4.5. *Comments on the Kelvin–Helmholtz instability*

Experiments on shear-induced breaking in strongly nonlinear solitary waves show that the most unstable wavelength is 6–8 times the thickness of a thin pycnocline, with depth ratio $h_1/h_2 \simeq 5$ and $\Delta h/h_2 \simeq 1/4$ (Fructus *et al.* 2009, table 1). In the present interfacial calculations, where the most unstable wavelength is even shorter, values of $\Delta x_1/h_2$ are in the range above 0.5. The maximum wavenumber of $2\pi(N/4)/L_1$ (the energy for higher wavenumbers is padded to zero) corresponding to a shortest

https://doi.org/10.1017/jfm.2015.42 Published online by Cambridge University Press

wavelength of $4\Delta x_1 > 2h_2$ does not resolve the length scale of the Kelvin–Helmholtz instability in the present calculations. A different instability occurs during strong interfacial interactions with a shallow geometry, in the form of a collapse, overturning and subsequent mixing of the thin pycnocline, see Sveen *et al.* (2002, figure 6). This kind of instability is observed in the three-dimensional calculations for very strong forcing, where the interface touches the top of the bottom geometry (results not shown).

5. Comparison to laboratory experiments

The three-dimensional method using the quadratic approximation is used to simulate a set of laboratory experiments carried out by Maxworthy (1979). He investigated the generation of trains of solitary waves due to the barotropic tidal flow of a stratified fluid over a three-dimensional bottom topography. The experiments were performed in a square wave tank of side 245 cm filled with a fluid layer of depth 10 cm. The fluid layer had a stratification near the bottom, with a pycnocline centred around a level of approximately 0.6 cm above the bottom. We shall take the mid-level of the pycnocline at 0.6 cm as the reference depth and the length scale (h_2) in the computations. Topography in the form of a ridge with a horizontal rectangular top, 16 cm wide and 60 cm long, was applied in the experiments. The ridge had constant slopes to the sides, forming another rectangle of 30 cm × 76 cm at the base. The geometry was towed horizontally upside down in the top part of the fluid layer, driving the wave motion along the pycnocline. The time-varying speed $U(t) = U_m \sin \Omega t$ of the ridge was along the direction of its width (the x_1-direction), where U_m denotes the maximum speed and $2\pi/\Omega$ the cyclic (tidal) period. Upstream wave formation was investigated varying the Froude number $Fr = U_m/c_0$ (c_0 defined in (3.8)) and the non-dimensional ridge height d_m/H, where $H = h_1 + h_2$.

The layer depths of the two-fluid system, size of wave tank, shape and motion of the topography in the calculations are similar to those in the laboratory experiments. With $H = h_1 + h_2 = 10$ cm and $h_2 \simeq 0.6$ cm as reference depth, the depth ratio becomes $h_1/h_2 = 15.6$. The length of the wave tank of 245 cm becomes $408h_2$. The theoretical topography has width and length at the half-height of 20.4 cm $\simeq 34h_2$ and 67 cm $\simeq 112h_2$, respectively. The shape of the topography used in the computations is given by $\delta(x_1, x_2) = d_m f_1(x_1) f_2(x_2)$, where d_m denotes the maximum height and

$$f_1(x_1) = \tfrac{1}{4}[1 + \tanh((x_1 - x_1^a)/3.5h_2)][1 - \tanh((x_1 - x_1^b)/3.5h_2)], \tag{5.1}$$

$$f_2(x_2) = \tfrac{1}{4}[1 + \tanh((x_2 - x_2^c)/3.5h_2)][1 - \tanh((x_2 - x_2^d)/3.5h_2)], \tag{5.2}$$

where $x_1^b - x_1^a = 34h_2$ and $x_2^d - x_2^c = 112h_2$. The excursion of the ridge after a half-period, corresponding to $2U_m/\Omega$, can be estimated from the experimental results. The velocity U_m is obtained from the Froude number $Fr = U_m/c_0$, which is given in the experiments. The experimental density stratification is used to estimate c_0. In non-dimensional terms, $\Omega h_2/c_0 \simeq 1/70$ can be estimated from the experiments and is used in the simulations. The numerical wave tank extends horizontally $400h_2$ by $400h_2$, with 500 nodes in each direction ($\Delta x_1 = \Delta x_2 = 0.8h_2$). The topography is moved according to $U(t)/c_0 = Fr \sin \Omega t$ for Ωt between 0 and π, and is stopped for $\Omega t > \pi$. The time step is $\Delta t = 0.22h_2/c_0$.

Maxworthy plotted his experimental results for the occurrence of the wave formation in the $(1 - d_m/H, Fr)$-plane. Waves occurred when Fr exceeded the straight line between the points $(1 - d_m/H, Fr) = (0.33, 0.36)$ and $(1 - d_m/H, Fr) = (0.6, 0.46)$,

https://doi.org/10.1017/jfm.2015.42 Published online by Cambridge University Press

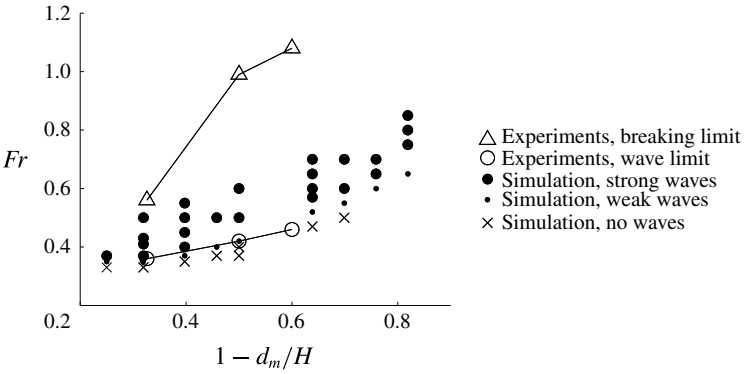


FIGURE 6. Comparison between experiments carried out by Maxworthy (1979) and numerical simulations using the present method, on the occurrence of internal waves in a layered fluid driven by a sinusoidally oscillating bottom topography as a function of the bottom topography height d_m and Froude number $Fr = U_0/c_0$. Depth ratio $h_1/h_2 = 15.6$. $\Omega h_2/c_0 = 1/70$. $H = h_1 + h_2$. Experimental wave limit (○) and breaking limit (△). Computational strong waves with amplitude $O(h_2)$ (●); weak waves with wave height $\sim 0.2h_2$ (•; see the definition in the main text); no waves (×).

with experimental error bars of $Fr = \pm 0.025$ (Maxworthy 1979, figure 6). The experimental transition line is indicated in the present figure 6. He also investigated the occurrence of wave breaking, also indicated in the figure.

Weak wave formation appears in the computations when a certain value of the Froude number is exceeded, corresponding exactly to the experiments carried out by Maxworthy (figure 6). His transition line for the onset of wave formation is further explored and extended here. Two calculated examples of weak wave trains at half-period ($\Omega t = \pi$), both with leading trough-to-crest height of $0.2h_2$, for a small Froude number of $Fr = 0.35$ in both cases, are shown in figures 7(*a*) and 8(*a*), for $1 - d_m/H = 0.32$ and 0.25, respectively. The leading trough-to-crest height almost doubles for the somewhat stronger $Fr = 0.37$ (figures 7*b*, 8*b*) and becomes comparable to the layer depth h_2 for the even stronger $Fr = 0.41$ (figure 7*c*). Appreciable wave height occurs for the much larger Froude number of $Fr = 0.8$ when the height d_m/H is small (figure 8*c*). Occurrences of weak wave trains (of wave height $\sim 0.2h_2$) for other values of Fr and d_m are indicated by the small dots in figure 6. Simulations with too small a Froude number or too small a topography height show no formation of a wave train, as indicated by the crosses in the figure. The present two-layer simulations with 40 different combinations of $0.25 < 1 - d_m/H < 0.82$ and $0.33 < Fr < 0.85$ confirm and extend the threshold of the wave formation as found experimentally by Maxworthy.

We have not investigated wave generation near the breaking limit in Maxworthy's experiments, which would require calculation of the fully nonlinear integral equations (2.3) and (2.4).

Direct comparisons between experiment and calculation of the generated wave trains at time instants $\Omega t = \pi$ and 1.4π, for $Fr = 0.5$ and $d_m/H = 0.5$, are shown in figure 9. The leading wave trough is ahead of the topography by approximately half the length of the topography in figure 9(*a*). Six wave troughs are observed in the experiment, while the computation exhibits five troughs at $\Omega t = \pi$, six troughs at $\Omega t = 1.1\pi$ and seven troughs at $\Omega t = 1.2\pi$, see also figure 10(*c*,*d*). The leading wave trough is ahead of the topography by approximately the length of the topography at the later time

https://doi.org/10.1017/jfm.2015.42 Published online by Cambridge University Press

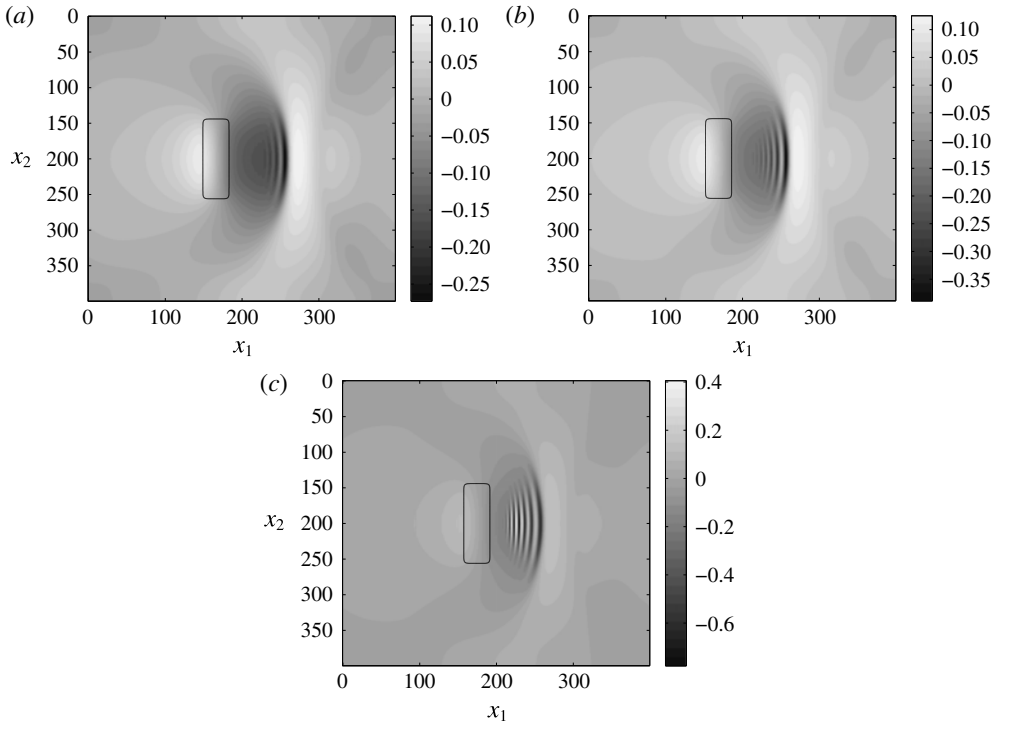


FIGURE 7. Interfacial elevation η/h_2 at $\Omega t = \pi$ (half-period) for $1 - d_m/H = 0.32$. (*a*) $Fr = 0.35$, (*b*) $Fr = 0.37$, (*c*) $Fr = 0.41$. $\Omega h_2/c_0 = 1/70$. Same resolution and shape of the geometry as in figure 6. Position of geometry, at half-height, at $\Omega t = \pi$, indicated.

$\Omega t = 1.4\pi$ (figure 9*b*). The computation then exhibits 10 wave troughs with a trough-to-trough wavelength of $4.8h_2$ in the back part of the wave train, which is moving with the group velocity, see also figure 10(*e*). The number of waves indicated from the experiment is five (figure 9*b*, right plot). (Note that the geometry is not moving for $\Omega t \geqslant \pi$.)

Figure 10 plots the calculated wave elevation along the mid-section of the tank ($x_2 = 200h_2$) as function of x_1 at different times during the wave generation process, $0.6\pi \leqslant \Omega t \leqslant 1.4\pi$. The location of the topography is indicated by the coordinates x_1^a and x_1^b, where $x_1^b - x_1^a = 34h_2$, see (5.1). The wave formation begins when the interface is sufficiently steep, at the leading face of the obstacle, for $\Omega t = 0.6\pi$. Two troughs are formed at $\Omega t = 0.7\pi$ and three at $\Omega t = 0.8\pi$. The number of waves behind the leading trough increases with time. So also does the trough-to-trough wavelength. The trough-to-crest height of the leading wave is $0.67h_2$ at $\Omega t = \pi$ and reduces to $0.59h_2$ at 1.4π. The leading wave widens monotonically. However, the wave is far more narrow than a two-dimensional fully nonlinear solitary wave of corresponding amplitude (figure 10*e*). The speed of the leading depression is supercritical for $\Omega t > 0.8\pi$, where the reference speed $\tilde{c}_0$ is calculated from the depth ratio at the positive elevation preceding the leading trough. At $\Omega t = 1.4\pi$ the excess speed of the leading depression, $\dot{X}_{trough}/\tilde{c}_0 - 1$, is approximately half the perfect solitary wave excess speed, as illustrated in figure 11. The differences in the wave shape and propagation speed of the three-dimensional transient wave and the perfect solitary wave in two dimensions illustrate differences in the three- and two-dimensional wave generation processes. The lateral leakage of

https://doi.org/10.1017/jfm.2015.42 Published online by Cambridge University Press

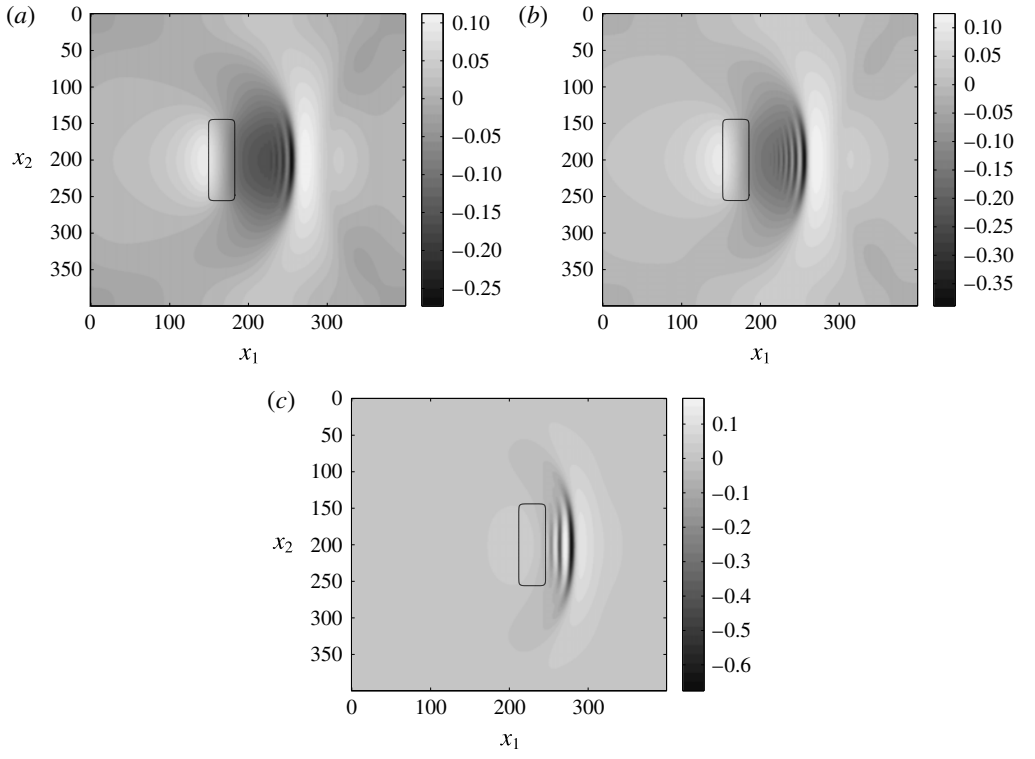


FIGURE 8. Interfacial elevation η/h_2 at $\Omega t = \pi$ (half-period). (*a*) $Fr = 0.35$, $1 - d_m/H = 0.25$. (*b*) $Fr = 0.37$, $1 - d_m/H = 0.25$. (*c*) $Fr = 0.8$, $1 - d_m/H = 0.82$. Same resolution and shape of the geometry as in figure 6. Position of geometry, at half-height, at $\Omega t = \pi$, indicated.

energy adds to the weakening of the leading trough in the three-dimensional case. The transient two-dimensional case is also slow in obtaining perfect solitary waves (Grue *et al.* 1997, figure 9). The fully nonlinear solitary wave calculation has been performed using the method in Grue *et al.* (1999) with a local reference level of $y_0 = 0.096h_2$, local depth ratio $(h_1 + y_0)/(h_2 - y_0) = 17.36$ and local amplitude $a/(h_2 - y_0) = 0.6527$. The soliton speed is 1.2399.

6. Simulations in relation to field measurements

Palmer *et al.* (2013) have measured strong internal waves generated along the seasonal thermocline at Jones Bank in the Celtic Sea. The spatio-temporal flow generated during the tidal cycle was in hydraulic control with supercritical velocity at the bank crest. A vertical depression of the thermocline, down to 40 m, corresponding to half the local water depth at the bank, was observed. In a complementary numerical study, Vlasenko *et al.* (2013) used the MITgcm-code to simulate two different wave scenarios in the field experiments, obtaining three wave trains per tidal cycle in each of them. The wave trains were sketched in Vlasenko *et al.* (2013, figures 6*a*, 11); no direct wave calculations were presented.

The observations by Palmer *et al.* (2013) and the simulations by Vlasenko *et al.* (2013) have motivated the model calculations of the temporal three-dimensional flow

https://doi.org/10.1017/jfm.2015.42 Published online by Cambridge University Press

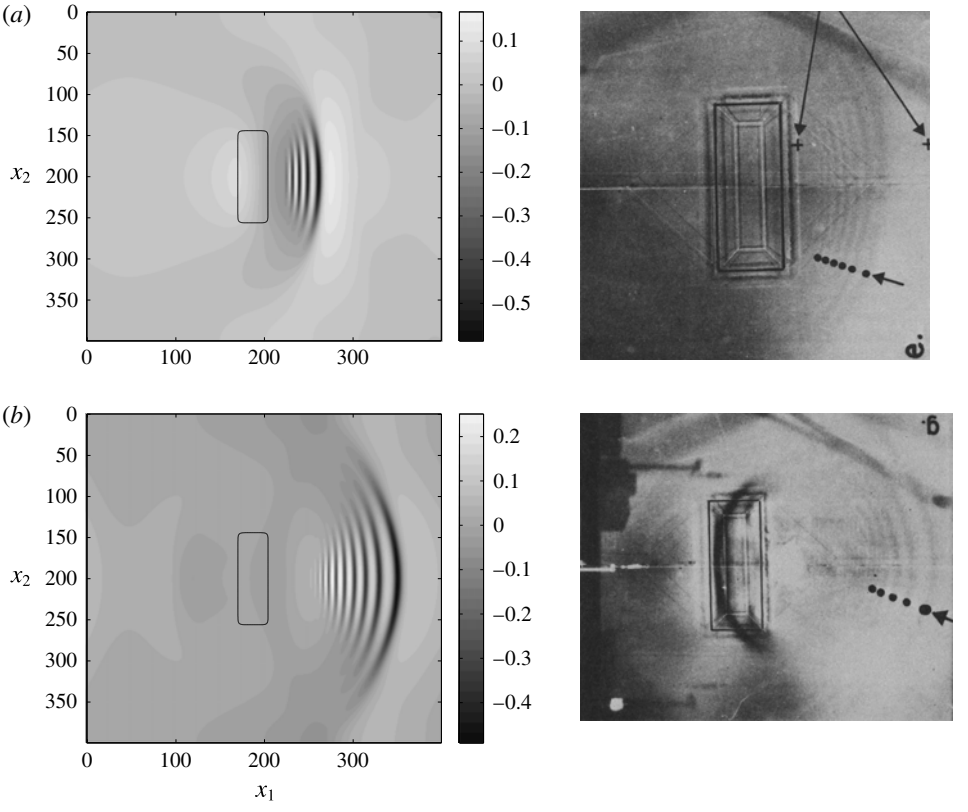


FIGURE 9. (*a*) Wave formation at (*a*) $\Omega t = \pi$ (half-cycle), computation (left), experiment by Maxworthy (1979, figure 8*e*) (right), (*b*) $\Omega t = 1.4\pi$, computation (left), experiment by Maxworthy (1979, figure 9*g*) (right). $Fr = 0.5$, $d_m/H = 0.5$, $\Omega h_2/c_0 = 1/70$.

features at the bank. We note that the present model does not take into account the rotational effects which are present in the oceanic setting. While the wave generation simulations during a short time frame may be realistic, the subsequent wave evolution is modified by rotational effects, see also the discussion in § 3.1.1 above.

The stratified sea has a thermocline with an average depth of approximately 40 m and is taken as the upper layer depth, i.e. $h_2 = 40$ m. The value of $c_0 \simeq 0.45$ m s^{-1} is obtained from the stratification (Vlasenko *et al.* 2013, figure 3). The bank has a width at its half-height of approximately 4 km and length approximately three times the width. The non-dimensional width and length at the bank's half-height become $w = 100h_2$ and $l = 300h_2$, respectively. The model geometry of the bank is given by $\delta(x_1, x_2) = d_m \exp[-(|x_1 - x_{10}|/(w/2))^3 - (|x_2 - x_{20}|/(l/2))^3]$, where d_m denotes the height of the bank. This is 50 m, and in the calculations is set to $1.2h_2$. The horizontal location of the summit of the bank is determined by (x_{10}, x_{20}). In the present calculations we mimic the tidal flow by moving (x_{10}, x_{20}) in an elliptical fashion. The depth outside the bank of 130 m gives $h_1/h_2 = 2.25$.

The M_2-tide has velocities of $(u_1, u_2) = (0.224, 0.360)$ m s^{-1} along the (width, length)-directions of the bank, which in non-dimensional terms become $(u_1, u_2)/c_0 \sim (0.5, 0.8)$ (Palmer *et al.* 2013, figure 3 and table 1). Vlasenko *et al.* (2013) have stressed the importance of an additional background current of 0.05 m s^{-1}

https://doi.org/10.1017/jfm.2015.42 Published online by Cambridge University Press

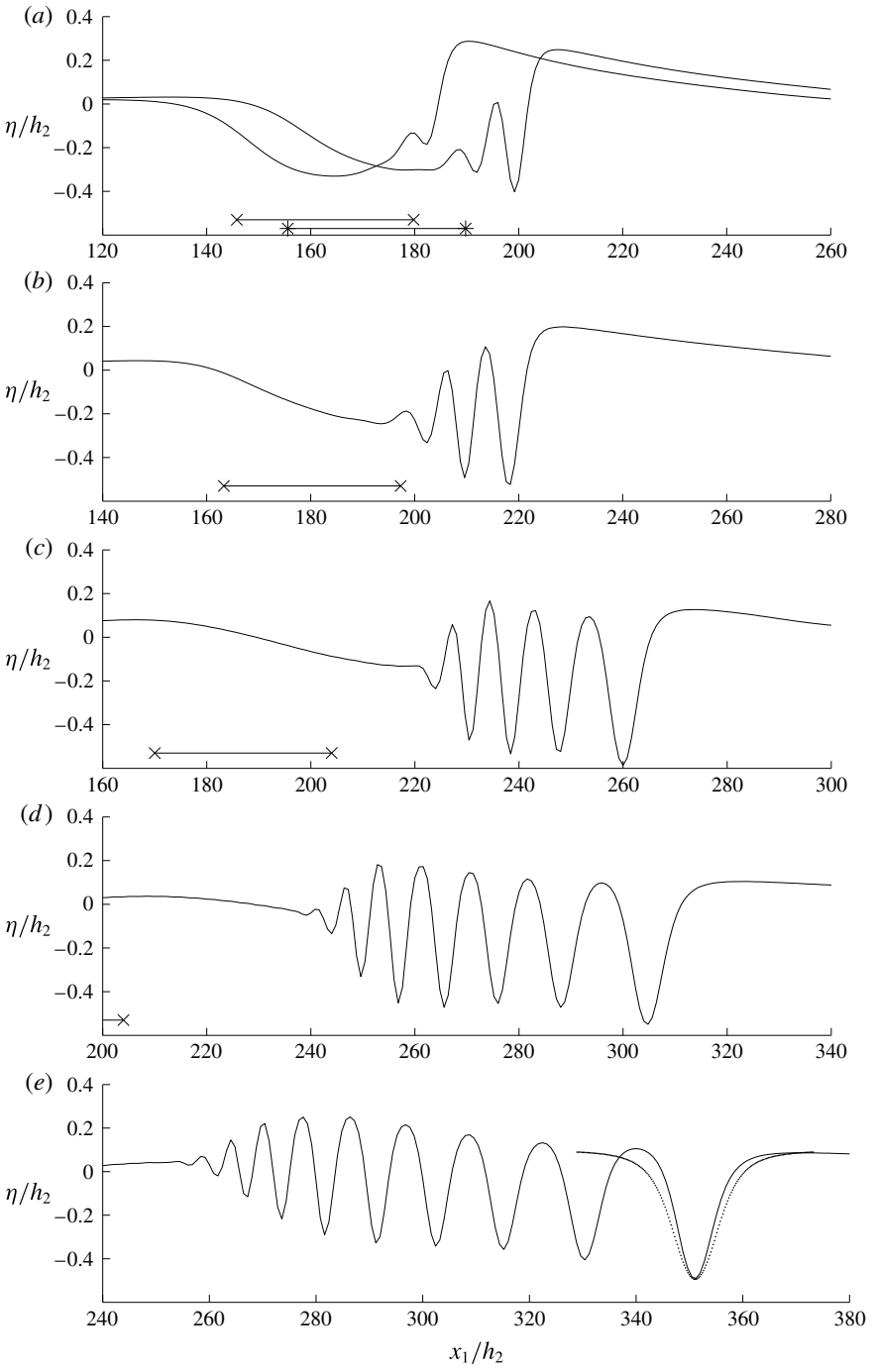


FIGURE 10. Elevation η at mid-section versus x_1 for fixed $x_2 = 200h_2$. (*a*) $\Omega t = 0.6\pi$ and 0.7π, (*b*) $\Omega t = 0.8\pi$, (*c*) $\Omega t = \pi$, (*d*) $\Omega t = 1.2\pi$, (*e*) $\Omega t = 1.4\pi$. Positions of x_a and x_b of geometry indicated by $\times$ ($\Omega t = 0.6\pi$, 0.8π, π) and $*$ (0.7π). $Fr = 0.5$, $d_m/H = 0.5$. Dotted line in (*e*) shows a two-dimensional fully nonlinear solitary wave calculation with a reference level of $y_0 = 0.096h_2$, depth ratio $(h_1 + y_0)/(h_2 - y_0) = 17.36$ and amplitude $a/(h_2 - y_0) = 0.6527$.

https://doi.org/10.1017/jfm.2015.42 Published online by Cambridge University Press

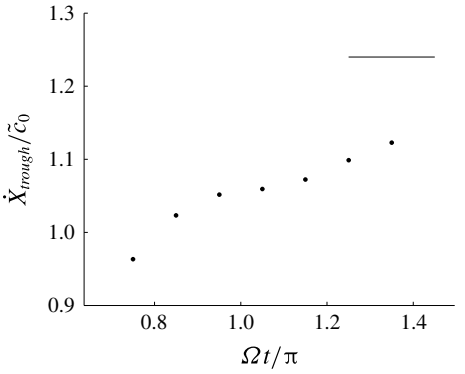


FIGURE 11. Speed of leading depression in figure 10 versus time (●). Speed of perfect two-dimensional solitary wave in figure 10(*e*) (——). Reference speed $\tilde{c}_0$ based on the layer depth at the maximum positive elevation preceding the leading trough.

across the bank, corresponding to an increase in $u_1/c_0 \simeq 0.1$. The effect of the background current is accounted for by increasing $(u_1, u_2)/c_0$ from (0.5, 0.8) to (0.6, 0.8) in the calculations below, where the model geometry is moved according to $(\dot{x}_{10}, \dot{x}_{20}) = (U_M \sin \Omega t, V_M \cos \Omega t)$. Both topography and fluid are initially at rest. A smooth ramp-up of $\dot{x}_{20}$ is employed. The computational domain is $400h_2$ by $600h_2$, with 720 nodes in each direction. The tidal frequency of $\Omega = 2\pi/12.4$ h^{-1} becomes in non-dimensional terms $\Omega h_2/c_0 \simeq 1/80$.

Simulations with $(u_1, u_2)/c_0 = (0.6, 0.8)$ show:

(i) For time $\Omega t = 0.6\pi$, $(\dot{x}_{10}, \dot{x}_{20})/c_0 = (0.57, -0.25)$, an elevation at $x_1 = 240h_2$ extends for $150h_2 < x_2 < 350h_2$ (figure 12*a*). A depression and a large bottom velocity is formed above the bank for $x_1 = 160h_2$ and $150h_2 < x_2 < 350h_2$. The bottom velocity, obtained in the frame of reference fixed to the bank, i.e. $\boldsymbol{v}_b = \boldsymbol{\nabla}\phi_1 - (\dot{x}_{10}, \dot{x}_{20})$ at B, is subcritical and up to $0.9c_0$ (figure 12*e*).

(ii) For $\Omega t = 0.8\pi$, $(\dot{x}_{10}, \dot{x}_{20})/c_0 = (0.35, -0.65)$, the elevation at $x_1 = 250h_2$–$260h_2$ and depression at $x_1 = 180$–$190h_2$ and $210h_2 < x_2 < 320h_2$ have slightly positive curvature in the x_1-direction (figure 12*b*). The bottom velocity is supercritical with a magnitude of up to $1.15c_0$ for $x_1 = 180h_2$–$190h_2$ and $230h_2 < x_2 < 320h_2$ (figure 12*f*). The region of supercritical velocity above the bank has a slight positive curvature in the x_1-direction.

(iii) For $\Omega t = 0.95\pi$, $(\dot{x}_{10}, \dot{x}_{20})/c_0 = (0.09, -0.79)$, a wave train appears behind the elevation at $x_1 = 270h_2$–$280h_2$. The curved depression over the bank at $x_1 = 200$–$220h_2$ and $230h_2 < x_2 < 320h_2$ is more pronounced (figure 12*c*). The three-dimensional region of supercritical bottom velocity (up to $1.2c_0$) is similarly curved (figure 12*g*).

(iv) For time $\Omega t = 1.15\pi$, $(\dot{x}_{10}, \dot{x}_{20})/c_0 = (-0.27, -0.71)$, the wave train behind the elevation at $x_1 = 320h_2$ has height up to $1.2h_2$. The crests are straight. A second wave train develops behind the interfacial trough previously located above the bank, now at $x_1 \sim 240h_2$. This wave train curves along the x_1-direction (figure 12*d*,*h*).

Simulations with the weaker excitation of $(u_1, u_2)/c_0 = (0.5, 0.8)$ show that for $\Omega t = 0.95\pi$, $(\dot{x}_{10}, \dot{x}_{20})/c_0 = (0.08, -0.79)$, a weak wave train develops behind the elevation at $x_1 = 270h_2$–$280h_2$. The much weaker depression over the bank at $x_1 = 210h_2$,

https://doi.org/10.1017/jfm.2015.42 Published online by Cambridge University Press

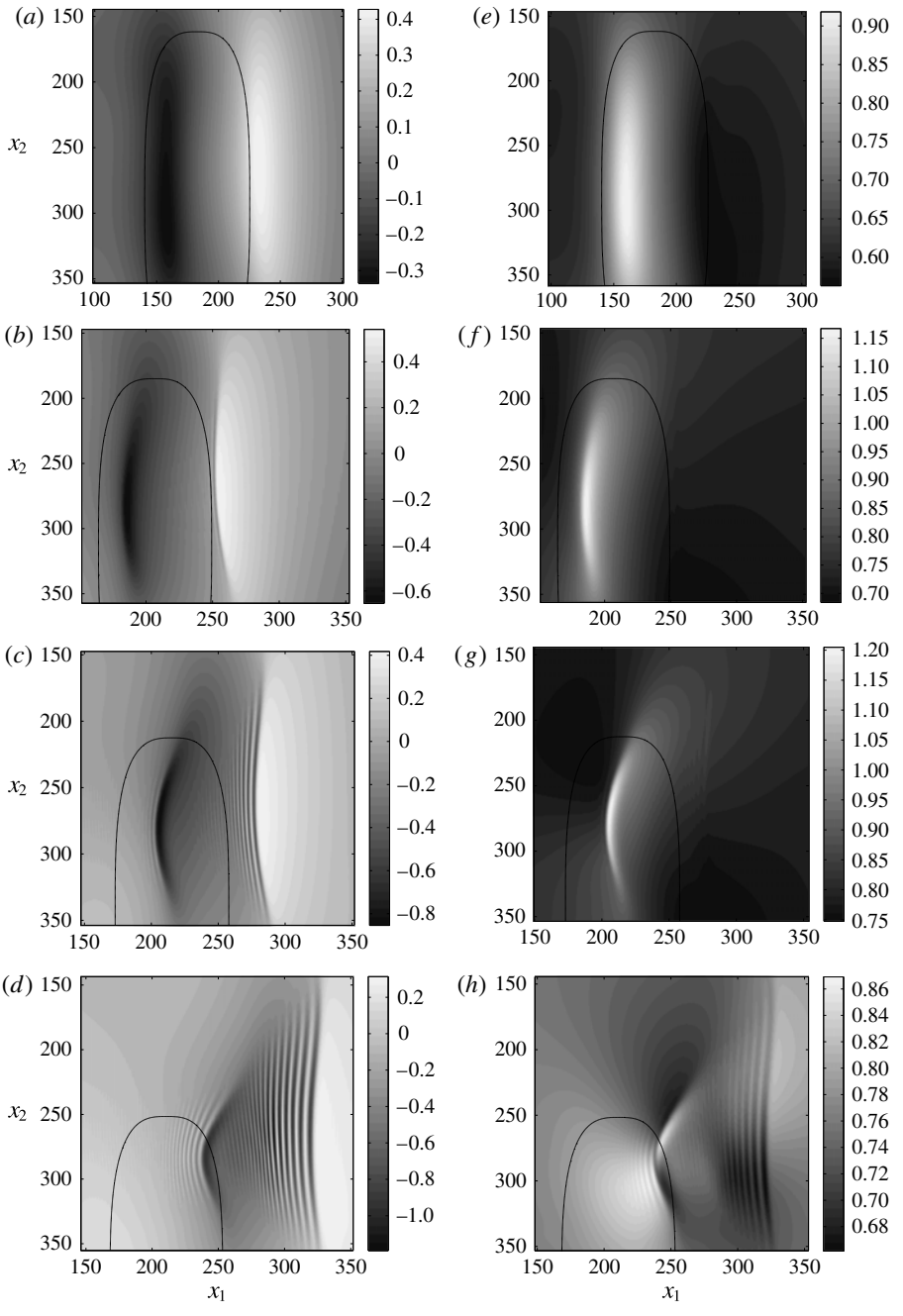


FIGURE 12. (*a–d*) Interfacial elevation η/h_2 and (*e–h*) bottom velocity $|\boldsymbol{v}_b|/c_0$, where $\boldsymbol{v}_b$ is the fluid velocity at the sea bottom, obtained in the frame of reference following the bank, for (*a,e*) $\Omega t = 0.6\pi$, (*b,f*) $\Omega t = 0.8\pi$, (*c,g*) $\Omega t = 0.95\pi$, (*d,h*) $\Omega t = 1.15\pi$. Current ellipse $(u_1, u_2)/c_0 = (0.6, 0.8)$. $h_1/h_2 = 2.25$, $d_m/h_2 = 1.2$, $\Omega h_2/c_0 = 1/86$. Position of topography indicated by the contour line at half-height. Velocity of topography $(\dot{x}_{10}, \dot{x}_{20})/c_0$ given in the main text.

https://doi.org/10.1017/jfm.2015.42 Published online by Cambridge University Press

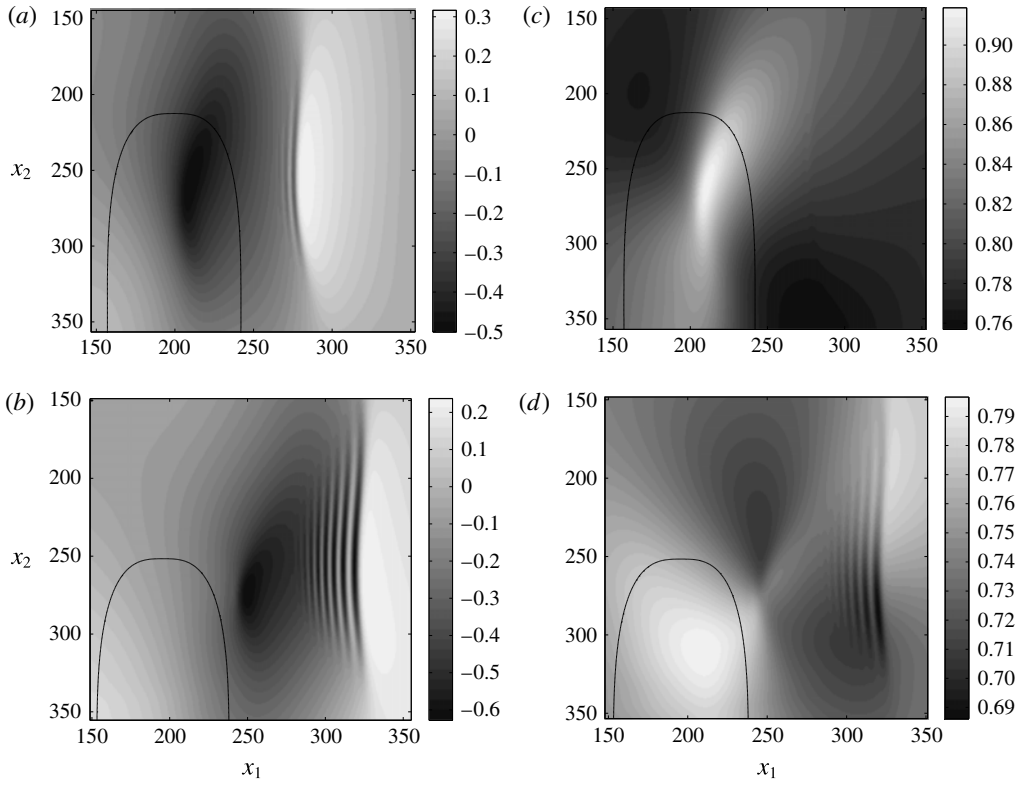


FIGURE 13. Same as figure 12 for $\Omega t = 0.95\pi$ (*a*,*c*); $\Omega t = 1.15\pi$ (*b*,*d*); current ellipse $(u_1, u_2)/c_0 = (0.5, 0.8)$.

$x_2 = 250h_2$ causes a subcritical bottom velocity (figure 13*a*,*c*). For time $\Omega t = 1.15\pi$ only one wave train behind the elevation, at $x_1 = 320h_2$ with height up to $0.8h_2$, is formed (figure 13*b*,*d*).

Sections of η/h_2, for fixed $x_2/h_2 = 280$, illustrate the two wave trains for the strong and weak excitations, obtained for $\Omega t = 0.95\pi$ and $\Omega t = 1.15\pi$. The wavelength is in the range $\lambda \sim 7h_2$–$3h_2$ (figure 14). The upstream wave train is much stronger than the downstream wave train, in the strong excitation. Only the upstream wave train is visible for the weak excitation. The leading depression of the dominant wave train in figure 14(*a*,*b*) moves a distance of approximately $40h_2$ between $\Omega t = 0.95\pi$ and $\Omega t = 1.15\pi$. The change in position is only slightly influenced by the topography. The other depression moves a distance of approximately $35h_2$ between $\Omega t = 0.95\pi$ and $\Omega t = 1.15\pi$. The local depth of the topography somewhat influences the wave propagation.

These model simulations show, for a time period somewhat longer than a half tidal cycle, i.e. $0 < \Omega t < 1.15\pi$, that two wave trains are generated for a tidal ellipse of strength $(u_1, u_2)/c_0 = (0.6, 0.8)$, and one wave train for $(u_1, u_2)/c_0 = (0.5, 0.8)$. The difference in u_1/c_0 between the two different scenarios corresponds to the small increase due to a background current of 0.05 m s^{-1} in the observations by Palmer *et al.* (2013) and simulations by Vlasenko *et al.* (2013). Thus, with a unidirectional background current across the bank, two wave trains are generated during the phase of strong excitation and one wave train during the phase of weak excitation – a total of three wave trains per tidal cycle.

https://doi.org/10.1017/jfm.2015.42 Published online by Cambridge University Press

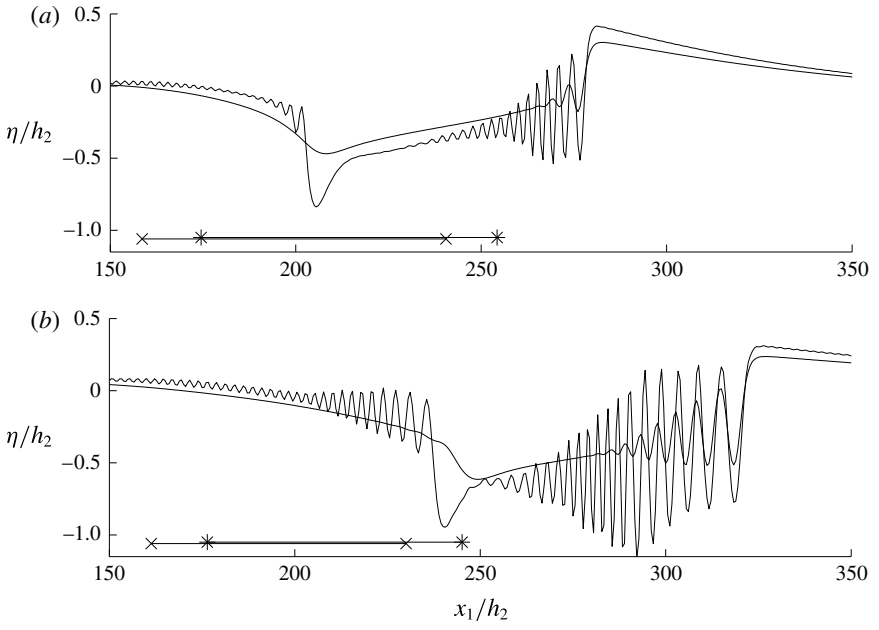


FIGURE 14. Interfacial elevation η/h_2. Section along $x_2 = 280h_2$, for strong $(u_1, u_2)/c_0 = (0.6, 0.8)$ and weak $(u_1, u_2)/c_0 = (0.5, 0.8)$ excitation. (*a*) $\Omega t = 0.95\pi$; (*b*) $\Omega t = 1.15\pi$. $h_1/h_2 = 2.25$, $d_m/h_2 = 1.2$. Horizontal position of the geometry at its half-height indicated by $*$—$*$ $(u_1, u_2)/c_0 = (0.6, 0.8)$, $\times$—$\times$ $(u_1, u_2)/c_0 = (0.5, 0.8)$.

7. Conclusion

We develop a two-layer mathematical interfacial wave model in three dimensions. The method is fully dispersive and strongly nonlinear and is here developed with complementary numerical implementation and testing. A set of integral equations couples the velocity potentials (tangential velocities) to the normal velocities along the lower and upper side of the interface. The interaction between the interfacial motion and a time-varying bottom topography is taken into account, where the bottom variation contributes to an additional coupled integral equation as well as integrals over the bottom variables.

The integral equations are at the onset fully nonlinear in the vertical excursions of the interface and bottom topography. The source and dipole terms appearing in the integral equations are developed in series expansions containing linear, quadratic, cubic and higher order terms. By means of successive approximations and application of the Fourier transform, explicit inversion of the integral equations is obtained in terms of series expansions. We find, for the applications in the present paper, calculating the formation of interfacial wave trains of non-dimensional amplitude up to unity, that the quadratic approximation contains the essential dynamics, while the additional cubic terms are very small. The quadratic and cubic approximations have been successfully compared to exact calculations of solitary waves over a flat bottom.

The three-dimensional method is used to calculate the curved wave train formation measured and visualized in experiments carried out by Maxworthy (1979), where a topography was moved in an oscillatory manner mimicking a tidal oscillation. The computations confirm the transition observed in the experiments: wave trains are formed when the Froude number (*Fr*) obtained from the maximum speed of the

https://doi.org/10.1017/jfm.2015.42 Published online by Cambridge University Press

topography divided by the linear internal long-wave speed exceeds a certain value, depending on the height of the geometry relative to the fluid layer depth. The leading depression wave is found to be narrower than a fully developed two-dimensional solitary wave of comparable amplitude, while the excess speed is approximately half that of the solitary wave.

We also perform a set of calculations relevant to tidally driven highly nonlinear and three-dimensional internal wave formation at the Jones Bank in the Celtic Sea. The calculations are motivated by recent field observations (Palmer *et al.* 2013) and numerical ocean modelling calculations (Vlasenko *et al.* 2013, 2014). Using the linear long-wave speed c_0 as the velocity scale, the tidal ellipse observed in the field becomes in non-dimensional terms $(u_1, u_2)/c_0 = (0.5, 0.8)$. The velocity components are across/along the bank. Simulations during a half tidal cycle, with two different tidal ellipses, of (0.6, 0.8) and (0.5, 0.8), show that two wave trains are formed in the former case and one wave train in the latter. One of the wave trains has forward curvature and is dictated by the curved strong depression over the bank. Rotational effects are not accounted for in the present model, see comments in § 3.1.1.

Appendix A. Expansions of the Green functions

The contributions from the Green function in (2.3) are expanded in power series of η and δ as

$$\frac{1}{r}+\frac{1}{r_1} = \frac{1}{R}+\frac{1}{R_1}+(\eta+\eta')\frac{\partial}{\partial(2h_1)}\frac{1}{R_1}-\frac{1}{2}(\eta-\eta')^2\nabla_H'^2\frac{1}{R} + \frac{1}{2}(\eta+\eta')^2\frac{\partial^2}{\partial(2h_1)^2}\frac{1}{R_1}+\cdots, \quad (\boldsymbol{x}, y) \text{ on } I, (\boldsymbol{x}', y') \text{ on } I, \tag{A 1}$$

$$\frac{1}{r}+\frac{1}{r_1} = \frac{2}{R_0}+2\eta\frac{\partial}{\partial h_1}\frac{1}{R_0}+(\eta^2+\delta'^2)\frac{\partial^2}{\partial h_1^2}\frac{1}{R_0}+\cdots, \quad (\boldsymbol{x}, y) \text{ on } I, (\boldsymbol{x}', y') \text{ on } B, \tag{A 2}$$

$$\left(\frac{\partial}{\partial y'}-\nabla_H'\eta'\cdot\nabla_H'\right)\left(\frac{1}{r}+\frac{1}{r_1}\right) = \frac{\partial}{\partial(2h_1)}\frac{1}{R_1}-\nabla_H'\cdot\left((\eta'-\eta)\nabla_H'\frac{1}{R}\right) - \nabla_H'\cdot\left((\eta'+\eta)\nabla_H'\frac{1}{R_1}\right) - \nabla_H'\cdot\left(\frac{1}{2}(\eta'+\eta)^2\nabla_H'\frac{\partial}{\partial(2h_1)}\frac{1}{R_1}\right)+\cdots, \quad (\boldsymbol{x}, y) \text{ on } I, (\boldsymbol{x}', y') \text{ on } I, \tag{A 3}$$

$$\left(-\frac{\partial}{\partial y'}+\nabla_H'\delta'\cdot\nabla_H'\right)\left(\frac{1}{r}+\frac{1}{r_1}\right) = 2\nabla_H'\cdot\left(\delta'\nabla_H'\frac{1}{R_0}\right) + 2\eta\nabla_H'\cdot\left(\delta'\nabla_H'\frac{\partial}{\partial h_1}\frac{1}{R_0}\right)+\cdots, \quad (\boldsymbol{x}, y) \text{ on } I, (\boldsymbol{x}', y') \text{ on } B. \tag{A 4}$$

In (A 1)–(A 4), $R_1=\sqrt{R^2+4h_1^2}$ and $R_0=\sqrt{R^2+h_1^2}$. ∇_H denotes horizontal gradient.

https://doi.org/10.1017/jfm.2015.42 Published online by Cambridge University Press

The contributions from the Green function in (2.4) are expanded similarly in η and δ as

$$\frac{1}{r}+\frac{1}{r_{1B}} = \frac{1}{R}+\frac{1}{R_1}-(\delta'+\delta)\frac{\partial}{\partial(2h_1)}\frac{1}{R_1} - \frac{1}{2}(\delta'-\delta)^2\nabla_H'^2\frac{1}{R}+\frac{1}{2}(\delta'+\delta)^2\frac{\partial^2}{\partial(2h_1)^2}\frac{1}{R_1}+\cdots, \quad (\boldsymbol{x},y)\ \text{on}\ B,\ (\boldsymbol{x}',y')\ \text{on}\ B, \tag{A 5}$$

$$\frac{1}{r}+\frac{1}{r_{1B}} = \frac{2}{R_0}-2\delta\frac{\partial}{\partial h_1}\frac{1}{R_0}+(\delta^2+\eta'^2)\frac{\partial^2}{\partial h_1^2}\frac{1}{R_0}+\cdots, \quad (\boldsymbol{x},y)\ \text{on}\ B,\ (\boldsymbol{x}',y')\ \text{on}\ I, \tag{A 6}$$

$$\left(-\frac{\partial}{\partial y'}+\nabla_H'\delta'\cdot\nabla_H'\right)\left(\frac{1}{r}+\frac{1}{r_{1B}}\right) = \frac{\partial}{\partial(2h_1)}\frac{1}{R_1}+\nabla_H'\cdot\left((\delta'-\delta)\nabla_H'\frac{1}{R}\right) + \nabla_H'\cdot\left((\delta'+\delta)\nabla_H'\frac{1}{R_1}\right) - \nabla_H'\cdot\left(\frac{1}{2}(\delta'+\delta)^2\nabla_H'\frac{\partial}{\partial(2h_1)}\frac{1}{R_1}\right)+\cdots \quad (\boldsymbol{x},y)\ \text{on}\ B,\ (\boldsymbol{x}',y')\ \text{on}\ B, \tag{A 7}$$

$$\left(\frac{\partial}{\partial y'}-\nabla_H'\eta'\cdot\nabla_H'\right)\left(\frac{1}{r}+\frac{1}{r_{1B}}\right) = -2\nabla_H'\cdot\left(\eta'\nabla_H'\frac{1}{R_0}\right) - 2\delta\nabla_H'\cdot\left(\eta'\nabla_H'\frac{\partial}{\partial h_1}\frac{1}{R_0}\right)+\cdots \quad (\boldsymbol{x},y)\ \text{on}\ B,\ (\boldsymbol{x}',y')\ \text{on}\ I. \tag{A 8}$$

Appendix B. Expressions for $V_I^{(3)}$ and $W_I^{(3)}$

The normal velocity V_I defined in (2.5) is obtained by the method of successive approximations, where $V_I = V_I^{(1)}+V_I^{(2)}+V_I^{(3)}+\cdots$, see § 2.2.3. $V_I^{(1)}$ and $V_I^{(2)}$ are obtained in (2.10) and (2.11) and $V_I^{(3)}$ as

$$\hat{V}_I^{(3)} = \frac{k}{1+e_1}(\hat{V}_I^{(3,1)}+\hat{V}_I^{(3,2)}+\hat{V}_I^{(3,3)}+\hat{V}_I^{(3,4)}), \tag{B 1}$$

$$\hat{V}_I^{(3,1)} = e_1\mathscr{F}[\eta(V_I-V_I^{(1)})]+\mathscr{F}\{\eta\mathscr{F}^{-1}[e_1(\hat{V}_I-\hat{V}_I^{(1)})]\}, \tag{B 2}$$

$$\hat{V}_I^{(3,2)} = -\tfrac{1}{2}k(1+e_1)\mathscr{F}(\eta^2V_I)+\mathscr{F}\{\eta\mathscr{F}^{-1}[k(1-e_1)\mathscr{F}(\eta V_I)]\} - \tfrac{1}{2}\mathscr{F}\{\eta^2\mathscr{F}^{-1}[k(1+e_1)\hat{V}_I]\}, \tag{B 3}$$

$$\hat{V}_I^{(3,3)} = \tfrac{1}{2}e_1\mathrm{i}\boldsymbol{k}\cdot\mathscr{F}(\eta^2\nabla_H\phi_{1I})+\mathscr{F}\{\eta\mathscr{F}^{-1}[e_1\mathrm{i}\boldsymbol{k}\cdot\mathscr{F}(\eta\nabla_H\phi_{1I})]\} - \tfrac{1}{2}\mathscr{F}[\eta^2\mathscr{F}^{-1}(e_1k^2\hat{\phi}_{1I})], \tag{B 4}$$

$$\hat{V}^{(3,4)} = -\mathscr{F}(\eta^2\mathscr{F}^{-1}[k\sqrt{e_1}\hat{V}_B])-k\sqrt{e_1}\mathscr{F}(\delta^2V_B) - \mathscr{F}(\eta\mathscr{F}^{-1}[2\sqrt{e_1}\mathrm{i}\boldsymbol{k}\cdot\mathscr{F}(\delta\nabla_H\phi_{1B})]), \tag{B 5}$$

where in (B 1)–(B 5) a hat denotes Fourier transform and $e_1=\mathrm{e}^{-2kh_1}$.

https://doi.org/10.1017/jfm.2015.42 Published online by Cambridge University Press

The normal velocity $W_I = W_I^{(1)} + W_I^{(2)} + W_I^{(3)} + \cdots$ defined in § 2.2.4 is obtained similarly, with $W_I^{(1)}$ and $W_I^{(2)}$ obtained in (2.14) and (2.15) and $W_I^{(3)}$ as

$$\hat{W}_I^{(3)} = \frac{k}{1+e_2}\left(\hat{W}_I^{(3,1)} + \hat{W}_I^{(3,2)} + \hat{W}_I^{(3,3)}\right), \tag{B 6}$$

$$\hat{W}_I^{(3,1)} = -e_2\mathscr{F}[\eta(W_I - W_I^{(1)})] - \mathscr{F}\{\eta\mathscr{F}^{-1}[e_2(\hat{W}_I - \hat{W}_I^{(1)})]\}, \tag{B 7}$$

$$\begin{aligned}\hat{W}_I^{(3,2)} = {} & -\tfrac{1}{2}k(1+e_2)\mathscr{F}(\eta^2 W_I) + \mathscr{F}\{\eta\mathscr{F}^{-1}[k(1-e_2)\mathscr{F}(\eta W_I)]\} \\ & -\tfrac{1}{2}\mathscr{F}\{\eta^2\mathscr{F}^{-1}[k(1+e_2)\hat{W}_I]\},\end{aligned} \tag{B 8}$$

$$\begin{aligned}\tfrac{1}{2}W_I^{(3,3)} = {} & -\tfrac{1}{2}e_2\mathrm{i}\boldsymbol{k}\cdot\mathscr{F}(\eta^2\boldsymbol{\nabla}_H\phi_{2I}) - \mathscr{F}\{\eta\mathscr{F}^{-1}[e_2\mathrm{i}\boldsymbol{k}\cdot\mathscr{F}(\eta\boldsymbol{\nabla}_H\phi_{2I})]\} \\ & +\tfrac{1}{2}\mathscr{F}[\eta^2\mathscr{F}^{-1}(e_2k^2\phi_{2I})],\end{aligned} \tag{B 9}$$

where a hat denotes Fourier transform and $e_2 = \mathrm{e}^{-2kh_2}$.

REFERENCES

BERNTSEN, J., XING, J. & DAVIES, A. M. 2008 Numerical studies of internal waves at a sill: sensitivity to horizontal size and subgrid scale closure. *Cont. Shelf Res.* **28**, 1376–1393.

BOEGMAN, L. & DOROSTKAR, A. 2011 Three-dimensional simulation of NLIW generation, propagation and breaking in Cayuga Lake. In *7th International Symposium Stratified Flows, Rome, Italy*, pp. 22–26.

CLAMOND, D., FRUCTUS, D. & GRUE, J. 2007 A note on time integrators in water-wave simulations. *J. Engng Maths* **58**, 149–156.

CLAMOND, D. & GRUE, J. 2001 A fast method for fully nonlinear water wave computations. *J. Fluid Mech.* **447**, 337–355.

FARMER, D. M. & ARMI, L. 1988 The flow of Atlantic water through the Strait of Gibraltar. *Prog. Oceanogr.* **21** (1), 1–105.

FRINGER, O. B., GERRITSEN, M. & STREET, R. L. 2006 An unstructured-grid finite-volume, nonhydrostatic, parallel coastal ocean simulator. *Ocean Model.* **14**, 139–173.

FRUCTUS, D., CARR, M., GRUE, J., JENSEN, A. & DAVIES, P. A. 2009 Shear induced breaking of large internal solitary waves. *J. Fluid Mech.* **620**, 1–29.

FRUCTUS, D., CLAMOND, D., GRUE, J. & KRISTIANSEN, Ø. 2005*a* An efficient model for three-dimensional surface wave simulations. Part I. Free space problems. *J. Comput. Phys.* **205**, 665–685.

FRUCTUS, D. & GRUE, J. 2007 An explicit method for the nonlinear interaction between water waves and variable and moving bottom topography. *J. Comput. Phys.* **222**, 720–739.

FRUCTUS, D., KHARIF, C., FRANCIUS, M., KRISTIANSEN, Ø., CLAMOND, D. & GRUE, J. 2005*b* Dynamics of crescent water wave patterns. *J. Fluid Mech.* **537**, 155–186.

GRIMSHAW, R. & HELFRICH, K. 2012 The effect of rotation on internal solitary waves. *IMA J. Appl. Maths* 1–14; doi:10.1093/imamat/hxs024.

GRUE, J. 2002 On four highly nonlinear phenomena in wave theory and marine hydrodynamics. *Appl. Ocean Res.* **24**, 261–274.

GRUE, J. 2013*a* Havets indre bølger. *Nature* **137** (6), 210–226; (in Norwegian).

GRUE, J. 2013*b* Interfacial wave motion of very large amplitude: formulation in three dimensions and numerical experiments. *Procedia IUTAM* **8**, 129–143; ISSN 2210-9838.

GRUE, J., FRIIS, H. A., PALM, E. & RUSÅS, P.-O. 1997 A method for computing unsteady fully nonlinear interfacial waves. *J. Fluid Mech.* **351**, 223–252.

GRUE, J., JENSEN, A., RUSÅS, P.-O. & SVEEN, J. K. 1999 Properties of large-amplitude internal waves. *J. Fluid Mech.* **380**, 257–278.

GRUE, J. & PALM, E. 1996 Wave drift damping of floating bodies in slow yaw motion. *J. Fluid Mech.* **319**, 323–352.

https://doi.org/10.1017/jfm.2015.42 Published online by Cambridge University Press

GRUE, J., PELINOVSKY, E. N., FRUCTUS, D., KHARIF, C. & TALIPOVA, T. 2008 Formation of undular bores and solitary waves in the Strait of Malacca caused by the 26 December 2004 Indian Ocean tsunami. *J. Geophys. Res.* **113**, C05008.

GUO, C., CHEN, X., VLASENKO, V. & STASHCHUK, N. 2011 Numerical investigation of internal solitary waves from the Luzon Strait: generation process, mechanism and three-dimensional effects. *Ocean Model.* **38**, 203–216.

JACKSON, C. R., DA SILVA, J. C., JEANS, G., ALPERS, W. & CARUSO, M. J. 2013 Nonlinear internal waves in synthetic aperture radar imagery. *Oceanography* **26**, 68–79.

LAI, Z., CHEN, C., COWLES, G. & BEARDSLEY, R. 2010 A nonhydrostatic version of FVCOM: 2. Mechanistic study of tidally generated nonlinear internal waves in Massachusetts Bay. *J. Geophys. Res.* **115**, C12049.

MAXWORTHY, T. 1979 A note on the internal solitary waves produced by tidal flow over a three-dimensional ridge. *J. Geophys. Res.* **84** (C1), 338–346.

MELVILLE, W. K. & HELFRICH, K. R. 1987 Transcritical two-layer flow over topography. *J. Fluid Mech.* **178**, 31–52.

MIKHLIN, S. G. 1957 *Integral Equations*, p. 338. Pergamon.

MOROZOV, E. G., PARRILLA-BARRERAB, G., VELARDE, M. G. & SCHERBININA, A. D. 2003 The straits of Gibraltar and Kara Gates: a comparison of internal tides. *Oceanol. Acta* **26** (3), 231–241.

NASH, J. D. & MOUM, J. N. 2005 River plumes as a source of large-amplitude internal waves in the coastal ocean. *Nat. Lett.* **437**, 400–403.

NEWMAN, J. N. 1977 *Marine Hydrodynamics*, p. 402. MIT Press.

OSTROVSKY, L. 1978 Nonlinear internal waves in a rotating ocean. *Oceanology* **18** (2), 119–125.

PALMER, M. R., INALL, M. E. & SHARPLES, J. 2013 The physical oceanography of Jones Bank: a mixing hotspot in the Celtic Sea. *Prog. Oceanogr.* **117**, 9–24.

SVEEN, J. K., GUO, Y., DAVIES, P. A. & GRUE, J. 2002 On the breaking of internal solitary waves at a rigde. *J. Fluid Mech.* **469**, 161–188.

VITOUSEK, S. & FRINGER, O. B. 2011 Physical vs. numerical dispersion in nonhydrostatic ocean modeling. *Ocean Model.* **40**, 72–86.

VLASENKO, V., SANCHEZ GARRIDO, J. C., STASHCHUK, N., GARCIA LAFUENTE, J. & LOSADA, M. 2009 Three-dimensional evolution of large-amplitude internal waves in the Strait of Gibraltar. *J. Phys. Oceanogr.* **39**, 2230–2246.

VLASENKO, V., STASHCHUK, N., INALL, M. E. & HOPKINS, J. 2014 Tidal energy conversion in a global hot spot: on the 3-D dynamics of baroclinic tides at the Celtic Sea shelf break. *J. Geophys. Res.* doi:10.1002/2013JC009708.

VLASENKO, V., STASHCHUK, N., PALMER, M. R. & INALL, M. E. 2013 Generation of barolinic tides over an isolated underwater bank. *J. Geophys. Res.* **118**, 1–14.

ZHANG, Z., FRINGER, O. B. & RAMP, S. R. 2011 Three-dimensional, nonhydrostatic numerical simulation of nonlinear internal wave generation and propagation in the South China Sea. *J. Geophys. Res.* **116**, C05022.

https://doi.org/10.1017/jfm.2015.42 Published online by Cambridge University Press